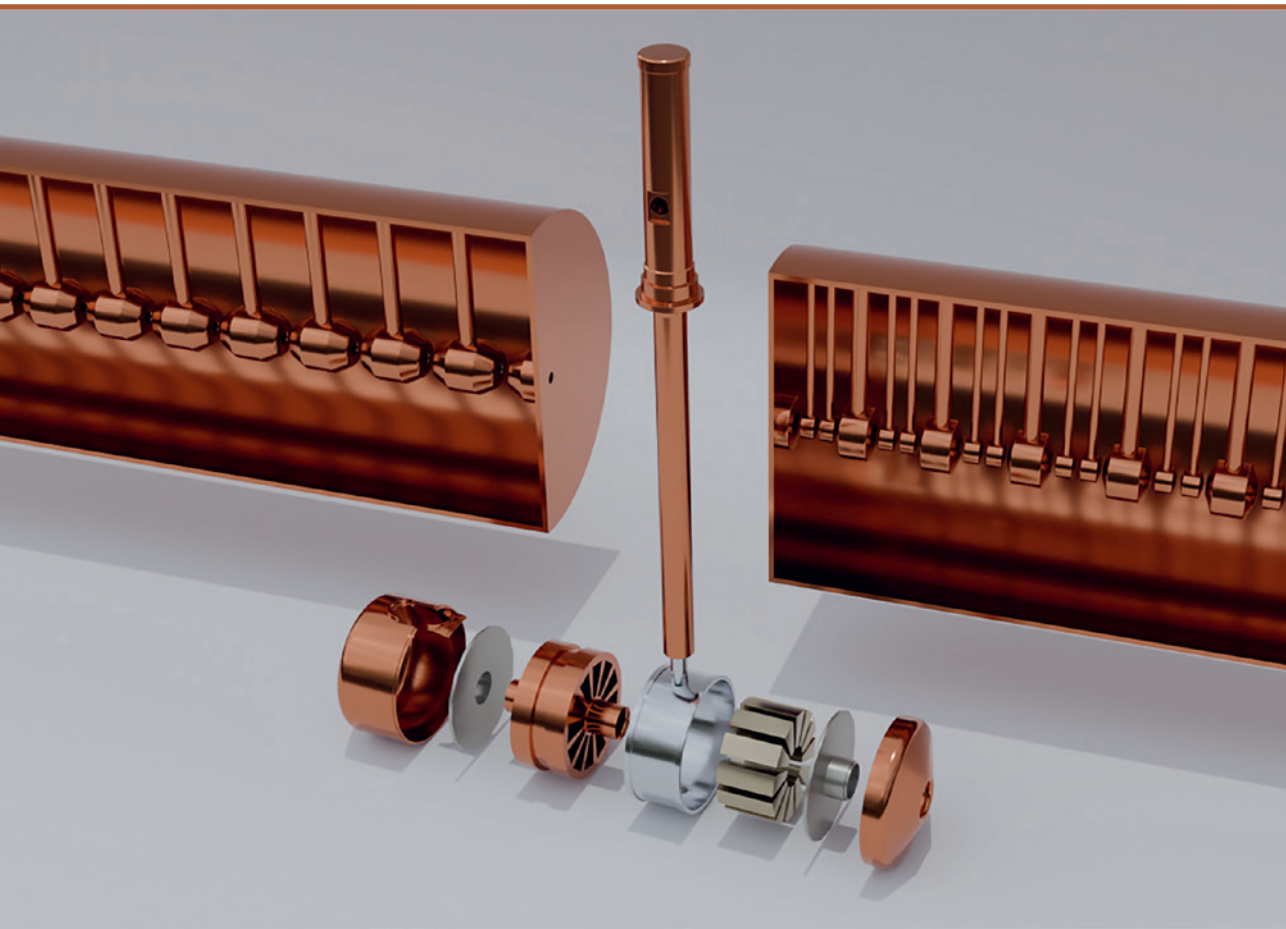
RIGA TECHNICAL UNIVERSITY

Lazar Nikitović

DEVELOPMENT OF LINEAR ACCELERATING STRUCTURES FOR ION INJECTION INTO A CANCER THERAPY SYNCHROTRON AND PARALLEL PRODUCTION OF RADIOISOTOPES

Summary of the Doctoral Thesis



RTU Press
Riga 2026

RIGA TECHNICAL UNIVERSITY
Faculty of Natural Sciences and Technology
Institute of Particle Physics and Accelerator Technologies

Lazar Nikitović
Doctoral Student of the Study Programme
"Particle Physics and Accelerator Technologies"

DEVELOPMENT OF LINEAR ACCELERATING STRUCTURES FOR ION INJECTION INTO A CANCER THERAPY SYNCHROTRON AND PARALLEL PRODUCTION OF RADIOISOTOPES

Summary of the Doctoral Thesis

Scientific supervisors

Dr. sc. ing.
TOMS TORIMS

Dr. phys.

MAURIZIO VRETENAR

RTU Press
Riga 2026

Nikitović, L. Development of Linear Accelerating Structures for Ion Injection into a Cancer Therapy Synchrotron and Parallel Production of Radioisotopes. Summary of the Doctoral Thesis. Riga: RTU Press, 2026, 71 p.

Published in accordance with the decision of the Promotion Council "RTU P-03" of 26 August 2026, Minutes No. 04030-9.3.2/5.

Research has been performed in collaboration with the European Organisation for Nuclear Research (CERN) *Next Ion Medical Machine Study* (NIMMS) group.





The research was carried out within the framework and with financial support of the following projects:

- State Research Programme (SRP) "High-energy physics and accelerator technologies" VPP-IZM-CERN-2020/1-0002; VPP-IZM-CERN-2022/1-0001;



- Horizon 2020 project "Heavy Ion Therapy Research Integration *plus*" (HITRI*plus*) WP7.4. This project has received funding from the European Union's Horizon 2020 Research and Innovation programme under grant agreement No. 101008548.



Cover photo was created by Lazar Nikitović
https://doi.org/10.7250/9789934373503
ISBN 978-9934-37-350-3 (pdf)

DOCTORAL THESIS PROPOSED TO RIGA TECHNICAL UNIVERSITY FOR PROMOTION TO THE SCIENTIFIC DEGREE OF DOCTOR OF SCIENCE

To be granted the scientific degree of Doctor of Science (PhD) in Physics and Astronomy, the present Doctoral Thesis has been submitted for defence at the open meeting of the RTU Promotion Council on 30 November 2026 at 15:00, Zoom online: https://rtucloud1.zoom.us/j/918551261387.

OFFICIAL REVIEWERS

Dr. **Giovanni Bisoffi**
National Institute for Nuclear Physics (INFN), Italy

Dr. **Jean-Baptiste Lallement**
European Organization for Nuclear Research (CERN), Switzerland

Prof. Dr. **Hendrik Hähnel**
Goethe University Frankfurt (GU), Germany

DECLARATION OF ACADEMIC INTEGRITY

I hereby declare that the Doctoral Thesis submitted for review to Riga Technical University for promotion to the scientific degree of Doctor of Science (PhD) is my own. I confirm that this Doctoral Thesis has not been submitted to any other university for promotion to a scientific degree.

Lazar Nikitović _____

Date: _____

The Doctoral Thesis has been written in English. It consists of 6 chapters, including Introduction and Conclusions, 88 figures, 36 tables, and 2 appendices; the total number of pages is 165, without appendices. The Bibliography contains 118 references.

LIST OF ABBREVIATIONS

Abbreviation	Meaning
AERT	Auger Electron-based Radioisotope Therapy
BEVA	Bevatech GmbH
BTL	Beam Transport Line
CCDTL	Cell-Coupled Drift Tube Linac
CERN	Conseil Européen pour la Recherche Nucléaire
CNAO	Centro Nazionale di Adroterapia Oncologica
DC	Direct Current
DEB	Debunching cavity
DT	Drift Tube
DTL	Alvarez Drift Tube Linac
EM	Electromagnetic
ERC	Energy Ramping Cavity
ESS	European Spallation Source
GUI	Graphical User Interface
HIT	Heidelberg Ion-beam Therapy Center
HITRI*plus*	Heavy Ion Therapy Research Integration *plus*
IAEA	International Atomic Energy Agency
IH-DTL	Interdigital H-mode Drift Tube Linac
KONUS	Combined zero degree structure
LANL	Los Alamos National Lab
MIT	Marburg Ion-beam Therapy Center
NIMMS	Next Ion Medical Machine Study
PET	Positron Emission Tomography
PMQ	Permanent Magnet Quadrupole
QA-DTL	Quasi-Alvarez Drift Tube Linac
RF	Radio Frequency
RHIC	Relativistic Heavy Ion Collider
S-IH-DTL	Separated function (tanks) Interdigital H-mode Drift Tube Linac
SEEIIST	South East European International Institute for Sustainable Technologies
SPECT	Single Photon Emission Computed Tomography
SSA	Solid State Amplifiers
SW	Standing Wave
TAT	Targeted Alpha Therapy
TE	Transverse Electric
TM	Transverse Magnetic
WP	Work Package

LIST OF SYMBOLS

Symbol	Meaning
$A_{xx'}$	– Area of the Twiss ellipse in horizontal phase space, mm.mrad
$\vec{B}$	– Magnetic induction vector, T
B_x	– Horizontal magnetic induction component, T
B_y	– Vertical magnetic induction component, T
B_z	– Axial magnetic induction component, T
C'_{dt}	– Production cost of one drift tubes, €
C_l	– Capital cost of accelerating structure, €/m
C_l^{DTL}	– Capital cost of DTL, €/m
C_l^{QA}	– Capital cost of QA-DTL, €/m
C_p	– Capital cost of radio-frequency system, €/W
C'_{pmq}	– Production cost of one permanent magnet quadrupoles, €
C'_{tank}	– Production cost per meter of cavity, €/m
C_{tot}	– Total cost of linac structure, €
E_0	– Average axial electric field amplitude, V/m
E_z	– Axial electric field component, V/m
L_c	– Length of the cell, m
L_f	– Flat edge length, m
L_g	– Gap length, m
L_s	– Stem diameter, m
N_{cell}	– Number of cells within the designed linac structure
N_p	– Number of particles inside the beam
P_b	– Beam power, W
P_d	– Power dissipation of a resonator, W
R_b	– Bore radius, m
R_{cav}	– Cavity radius, m
R_c	– Corner radius, m
R_{dt}	– Drift tube radius, m
R_i	– Inner nose radius, m
R_o	– Outer nose radius, m
T	– Transit-time factor
V_0	– Axial RF voltage, V
W_{IN}	– Input energy of linac structure, MeV
W_{OUT}	– Output energy of linac structure, MeV
W_{cur}	– Input energy of the designed cell, MeV
Z	– Effective shunt impedance, Ω
$ZT2_{best}$	– Maximum effective shunt impedance per unit length for the cell currently being designed, Ω/m

$ZT2_{cal}$	– Calculated effective shunt impedance per unit length within the designed cells, Ω/m
Z' or $ZT2$	– Effective shunt impedance per unit length, Ω/m
ΔW	– Energy the particle gains within a cell, MeV
$\Delta\phi_c$	– Phase shift between two neighboring cells, $^\circ$
$\alpha(s)$	– Alpha function, one of the three Twiss parameters
β	– Velocity of the particle relative to the speed of light in free space
$\beta(W_{cur})$	– Particle velocity corresponding to the W_{cur} energy
$\beta(s)$	– Beta function, one of the three Twiss parameters, mm/π.mrad
γ	– Face angle, $^\circ$
$\gamma(s)$	– Gamma function, one of the three Twiss parameters, π.mrad/mm
λ	– Radio frequency wavelength, m
ϕ	– Phase of the field relative to its crest, $^\circ$
ϕ_s	– Phase of the synchronous particle, $^\circ$
θ_e	– Angle of rotation of the Twiss ellipse, $^\circ$
ε	– Permittivity of a medium, F/m
$\varepsilon_{xx'}$	– Beam emittance in horizontal phase space, π.mm.mrad
f_{res}	– Resonant frequency, Hz
k_{ch}	– Auxiliary variable
l	– Length of the cylindrical resonator, m
n_p	– Periodicity factor within QA-DTL
$\vec{p_r}$	– Relativistic momentum vector of a particle in motion, kg·m/s
q	– Electric charge of the particle, C
s	– Beam abscissa within the linac structure, m
v	– Particle velocity, m/s
v_z	– Particle velocity in longitudinal direction, m/s

Table of Contents

1 General Outline of the Thesis **9**

1.1 Aim of the Doctoral Thesis 9
1.2 Hypothesis of the research 10
1.3 Scope of the Doctoral Thesis 10
1.4 Tasks of the Doctoral Thesis 10
1.5 Scientific novelty 10
1.6 Practical significance and applications 11
1.7 Approbation of the results 11

2 Linear Accelerating Structures for Medical Applications **13**

2.1 HITRI*plus* project 15
2.2 NIMMS collaboration 16
2.3 Radioisotope production with linac 17

3 RF and Beam Optics Theory of Linac Structures **19**

3.1 Electromagnetic field theory for linac structures 19
3.2 Beam optics for linac structures 22
3.3 Analyzed structures for acceleration and beam manipulation 25
3.4 Cost efficiency of Alvarez-type linac structures 31

4 Mathematical Model for Optimizing Geometry Parameters of Linac Structures **33**

4.1 Simulation software 33
4.2 Design procedures and optimization algorithms 34

5 Research Results **38**

5.1 HITRI*plus* carbon linac designs 38
5.1.1 Quasi-Alvarez Drift Tube Linac for carbon injection into synchrotron . 38
5.1.2 Alvarez Drift Tube Linac for radioisotope production 41
5.1.3 Debunching cavity before injection into carbon synchrotron 45
5.1.4 Comparison and choice of the ideal linac configuration 46
5.2 NIMMS helium linac designs 49

5.2.1 Quasi-Alvarez Drift Tube Linac for helium injection into synchrotron and radioisotope production 49
5.2.2 Alvarez Drift Tube Linac for radioisotope production 53
5.2.3 Debunching cavity and energy ramping cavity before injection into helium synchrotron 57
5.2.4 Comparison and choice of the ideal linac configuration 58
5.3 Isotope production helium linac design 60

6 Conclusions **63**
6.1 Thesis statements to be defended 64
6.2 Future research challenges 65

BIBLIOGRAPHY **66**

1. General Outline of the Thesis

1.1 Aim of the Doctoral Thesis

This Thesis aims to develop highly efficient novel linac structures to serve as injectors for particle therapy synchrotrons and then compare them with existing structures. The developed linac structures are designed to optimize power efficiency and beam quality compared to existing accelerators, ensuring improved performance in clinical settings. The ability to accelerate both carbon and helium ions within a single linac system enhances the flexibility and applicability of the design. The comparison of the developed linac structures with existing accelerators is followed by the selection of the most promising structure for the next-generation linacs.

Beyond its role in cancer treatment, the linac is also envisioned as a versatile system capable of supporting radioisotope production. The demand for medical radioisotopes, particularly for imaging and therapy treatments, continues to rise, necessitating reliable production methods. By enabling high-intensity, precise ion beam acceleration, the proposed linac structure can contribute to the production of radioisotopes commonly used in therapy and diagnostics.

A central objective of this research is to establish a systematic approach for developing an efficient linac structure tailored to the dual-purpose operation of synchrotron injection and radioisotope production. To achieve this, the study introduces a set of algorithms for developing linac structures aimed at maximizing the effective shunt impedance per unit length, an essential parameter influencing energy consumption and acceleration efficiency. These algorithms have been implemented in two graphical user interfaces (GUIs) created by the author, allowing for the automated development of linac structures.

Ultimately, this Thesis aims to contribute to the advancement of accelerator technology by providing a linac structure design that meets the evolving needs of modern particle therapy and radioisotope production. This research lays the groundwork for next-generation linacs capable of delivering high-quality ion beams with enhanced efficiency.

1.2 Hypothesis of the research

Building upon the knowledge of recently developed accelerator technologies and modern simulation codes, one can develop less expensive and more flexible linear accelerators than those used so far for ion injection into therapy synchrotrons, which can, at the same time, produce radioisotopes.

1.3 Scope of the Doctoral Thesis

The scope of the Thesis is to develop a novel standing-wave linac structure as an ion injector for cancer therapy synchrotrons that can reduce costs and improve performance with respect to currently used linac structures, and at the same time allow the production of radioisotopes.

1.4 Tasks of the Doctoral Thesis

In order to achieve the overall goal, the following tasks are established:

1. To investigate existing ion linac structures that could be used as a carbon and helium injector for a cancer therapy synchrotron.
2. To define an optimization methodology for designing linac structures, by maximizing power efficiency and ensuring beam transmission without any loss of particles.
3. To design and optimize different linac structures with the required input and output parameters, to be used as ion injectors for cancer therapy synchrotrons, or for the production of radioisotopes at different energies.
4. To compare the different linac structures designed under task three and select the overall best solution for future carbon and helium cancer therapy facilities.
5. To integrate the designed linac structures into the proposed helium and carbon ion therapy facilities.

1.5 Scientific novelty

This Thesis makes a significant contribution to accelerator technologies, with the most impactful achievements as follows:

1. A novel ion linac structure has been developed as an injector for cancer therapy synchrotrons, offering improved output beam parameters compared to currently used Interdigital H-mode Drift Tube Linac (IH-DTL) injectors.

2. The developed optimization tools are not limited to linac structures used as injectors for cancer therapy synchrotrons, but can also be applied to ion linac designs studied in other fields.

1.6 Practical significance and applications

1. The Alvarez-type linac configuration, composed of the developed Quasi-Alvarez Drift Tube Linac (QA-DTL) and two Alvarez Drift Tube Linac (DTL) cavities, offers a shorter, improved linac solution for future particle therapy facilities, providing higher beam quality with comparable power consumption to IH-DTL based solutions.

2. In a stand-alone, the proposed Alvarez-type linac configuration can be utilized for the production of innovative radioisotopes with a high-current beam at a lower cost compared to existing solutions.

3. The developed Alvarez-type linac configuration is part of the general design of the HITRI*plus* carbon linac[1] and the NIMMS helium linac[2]. Due to its performance presented in this Thesis, the developed linac configuration was chosen as the injector for the future Advanced Particle Therapy Center for the Baltic States[3].

1.7 Approbation of the results

Articles in peer-reviewed journals

1. **L. Nikitovic**, M. Vretenar, and T. Torims, "An Alvarez-type linac configuration for future carbon and helium ion therapy facilities with parallel radioisotope production", *Instruments* 2026; 10(1):16, https://doi.org/10.3390/instruments10010016

2. M. Vretenar, A. Lombardi, and **L. Nikitovic**, "A helium ion linear accelerator optimised for astatine production", *Instruments* 2026; 10(2):25, https://doi.org/10.3390/instruments10020025

Publications in conference proceedings

1. **L. Nikitovic**, T. Torims, and M. Vretenar, "Comparison of 352 MHz linac structures for injection into an ion therapy accelerator", Journal of Physics: Conference Series, Jan. 2024, pp. 1–8, https://doi.org/10.1088/1742-6596/2687/5/052011

[1]Website: https://www.hitriplus.eu
[2]Website: https://nimms.web.cern.ch
[3]Link: https://link.springer.com/article/10.1007/s12553-024-00875-2

2. **L. Nikitovic**, T. Torims, and M. Vretenar, "Design of a helium ion linear accelerator for injection in a particle therapy synchrotron and parallel production of radioisotopes", in Proc. LINAC2024, Chicago, IL, USA, Aug. 2024, pp. 147–150, https://doi.org/10.18429/JACoW-LINAC2024-MOPB045

3. M. Vretenar, A. Lombardi, and **L. Nikitovic**, "Design of a helium ion linear accelerator for astatine production", in Proc. IPAC25, Taipei, Taiwan, Jun. 2025, pp. 1044–1047, https://doi.org/10.18429/JACoW-IPAC2025-TUPB046

Presentations and seminars

1. "Comparison of Linac Structures for Injection into an Ion Therapy Accelerator and parallel production of radioisotopes", Joint NIMMS-SEEIIST Meeting #96, 14th Jul. 2023, https://indico.cern.ch/event/1306275/

2. "Linac design for HeLICS injector and for production of 211At", Internal NIMMS Meeting #51, 27th Sep. 2024, https://indico.cern.ch/event/1460836/

3. "Novel LINAC Design for Hadrontherapy and Radioisotope Production", MAPF meeting, 06.12.2023, https://indico.cern.ch/event/1217587/

Conference participation

1. 2nd CERN Baltic Conference (CBC 2022), oral presentation "Design of DTL for Acceleration of Ions with charge-to-mass Ratio of 1/2 with a Potential Production of Radioisotopes", 10–12 Oct. 2022, Vilnius, Lithuania, https://indico.cern.ch/event/1147717/

2. 3rd CERN Baltic Conference (CBC 2023), poster presentation "Comparison of different LINAC structures for injection into an ion therapy accelerator and parallel production of radioisotopes", 9–11 Oct. 2023, Riga, Latvia, https://indico.cern.ch/event/1288731/

3. 4th CERN Baltic Conference (CBC 2024), oral presentation "Novel linear accelerator design for injection of helium ions into a particle therapy synchrotron and parallel radioisotope production", 15–17 Oct. 2024, Tallinn, Estonia, https://indico.cern.ch/event/1416853/

4. 14th International Particle Accelerator Conference (IPAC'23), poster presentation "Comparison of 352 MHz LINAC structures for injection into an ion therapy accelerator", 7–12 May 2023, Venice, Italy, https://www.ipac23.org/

5. 3rd I.FAST Annual Meeting, discussions on novel linac designs, 16–19 Apr. 2024, Paris, France, https://indico.cern.ch/event/1357302/

2. Linear Accelerating Structures for Medical Applications

Linacs are used in standalone mode for various scientific and commercial applications, impacting our lives in many ways. Moreover, most circular particle accelerators require a linac as an injector, making it a crucial component. Today, there are more than 30,000 particle accelerators worldwide, of which half are radiotherapy electron linacs used in hospitals for the production of X-rays for cancer treatment [1].

Linacs used for the acceleration of heavier particles, which become relativistic only at high energy, such as protons and other ions heavier than protons, consist of a pre-accelerating and beam-bunching structure, usually a radio frequency quadrupole (RFQ), and one or more linac structures, depending on the application and the desired output energy, as shown in Fig. 2.1.

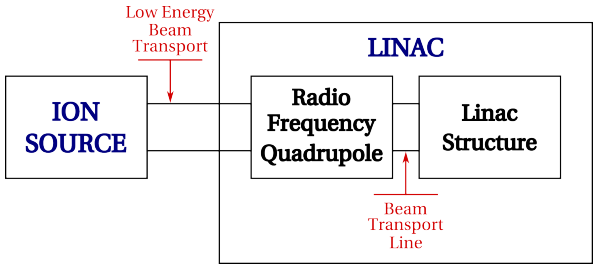


Fig. 2.1. Schematic representation of a typical ion source and linac configuration.

Usually, the criterion for choosing the most suitable linac structure for a given application is to select the most efficient option, based on the choice of the accelerated particle, energy range, and operational mode. For the medical application discussed in this Thesis, the candidates are the Alvarez Drift Tube Linac (DTL) and its modification, the Quasi-Alvarez Drift Tube Linac (QA-DTL), followed by the Interdigital H-mode Drift Tube Linac (IH-DTL) and its modification, the Separated tanks Interdigital H-mode Drift Tube Linac (S-IH-DTL).

The layout of a typical particle therapy facility, like the one in Heidelberg, is shown in Fig. 2.2, highlighting the position of the linac and its size in comparison to the other components of the facility.

The linac structure within a particle therapy center must be compact, energy-efficient, and have low operational and maintenance costs. The initial acceleration of protons or particles

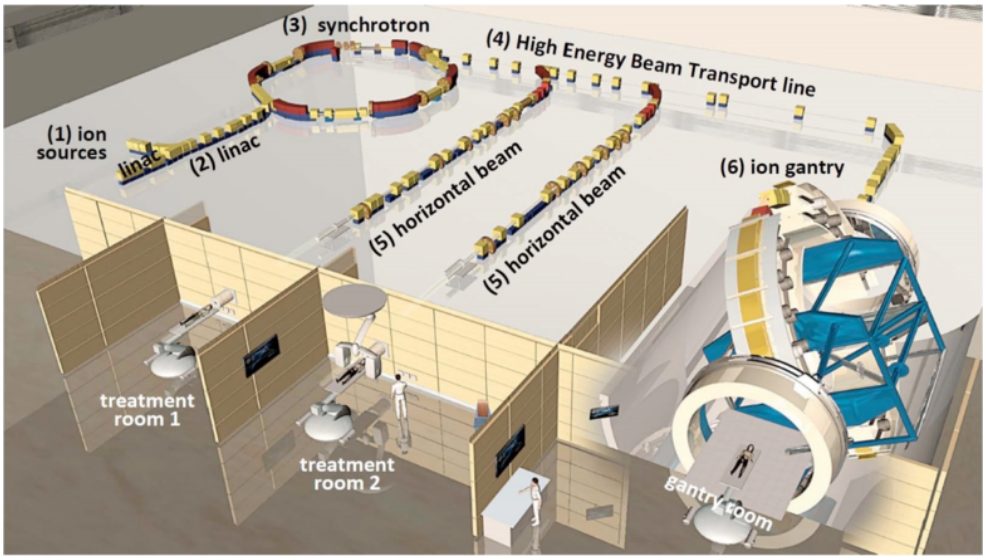


Fig. 2.2. Layout of the particle therapy facility in Heidelberg (Source: [2]).

heavier than protons within the particle therapy facilities nowadays is usually done with either the DTL or IH-DTL.

Only four particle therapy centers that use carbon ions for patient cancer treatments currently exist in Europe: MedAustron in Austria [3], Marburg Ion-beam Therapy Center (MIT) in Germany [4], Heidelberg Ion-beam Therapy Center (HIT) in Germany, and Centro Nazionale di Adroterapia Oncologica (CNAO) in Italy [5].

The IH-DTL along with its modification, the S-IH-DTL, are shown in Fig. 2.3.

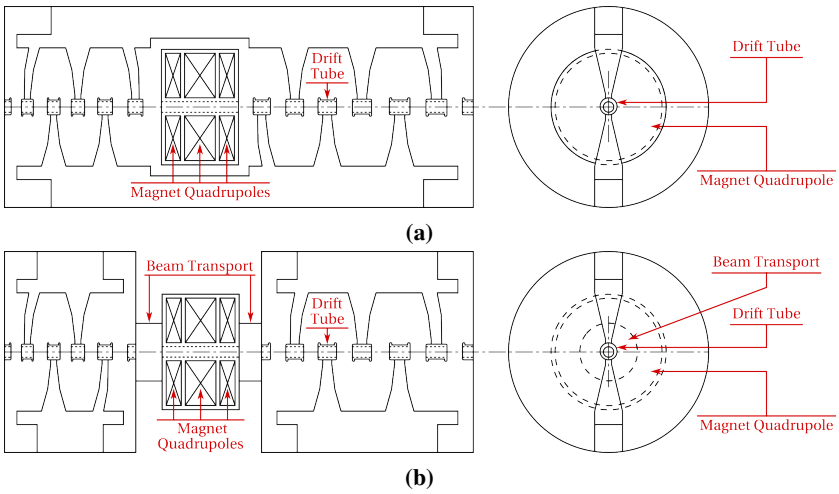


Fig. 2.3. Sections of the (a) IH-DTL and (b) S-IH-DTL linac structures.

In contrast, the DTL has proven to be a reliable linac structure through its implementation as a proton injector for synchrotrons in leading particle accelerator research facilities around the world, such as the *Conseil Européen pour la Recherche Nucléaire* (CERN) [6], the *Relativistic Heavy Ion Collider* (RHIC) [7], the *European Spallation Source* (ESS) [8], and others.

Unfortunately, the DTL has not received much recognition as a carbon injector for synchrotrons. Therefore, this Thesis aims to conduct a detailed study of the modified DTL, the QA-DTL, and emphasize its potential and the recognition it deserves as a synchrotron injector. The introduction of the QA-DTL will pave the way for the use of Alvarez-type structures as carbon injectors. The sections of the DTL and QA-DTL are shown in Fig. 2.4.

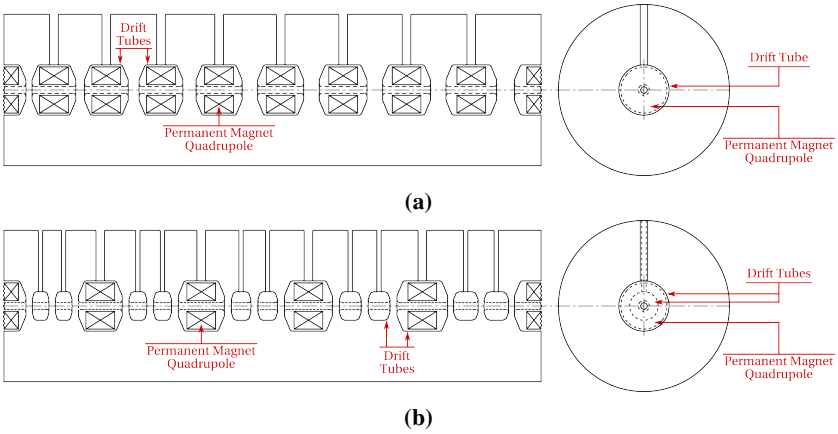


Fig. 2.4. Sections of the (a) DTL and (b) QA-DTL linac structures.

2.1 HITRI*plus* project

Heavy Ion Therapy Research Integration *plus* (HITRI*plus*) has the goal to integrate and propel medical and biophysics research on cancer treatment with heavy ion beams and at the same time develop its sophisticated instruments [9].

Specifically for this Thesis, the relevant Work Package (WP) is WP7, with a focus on Task 4. Task 7.4 addresses the improvement of injector linac design and is carried out by the Bevatech GmbH (BEVA) – CERN team, with contributions from the South East European International Institute for Sustainable Technologies (SEEIIST). The linac structure designs presented in this Thesis have been developed by the author according to the linac layout shown in Fig. 2.5.

The linac is composed of three distinct sections. The first section contains an RFQ and a linac structure of any type capable of accelerating both carbon and helium ions up to 5 MeV/u. The second and third sections contain only linac structures dedicated to accelerating helium ions from 5 MeV/u to 7.1 MeV/u and from 7.1 MeV/u to 10 MeV/u, respectively. The transition energy between the second and third sections is set at 7.1 MeV/u, primarily due to the production of 211-Astatine, one of the most promising alpha-emitting radioisotopes for cancer treatment [10].

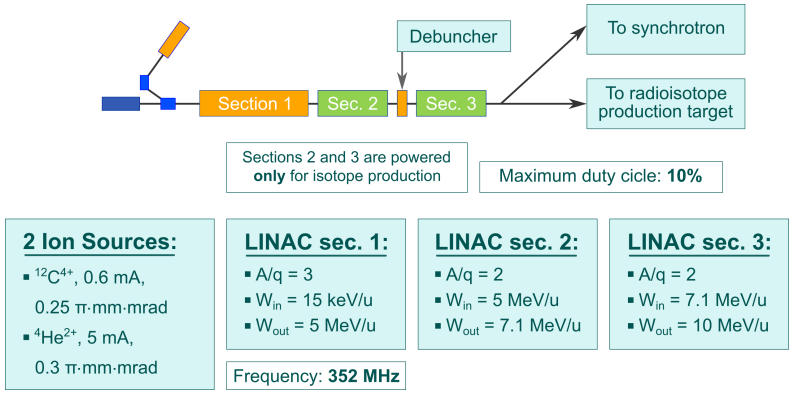


Fig. 2.5. Layout of the HITRI*plus* linac.

In other words, the first section serves solely as an injector for the therapy synchrotron, while the second and third sections are dedicated exclusively to radioisotope production.

2.2 NIMMS collaboration

In 2019, CERN launched the Next Ion Medical Machine Study (NIMMS) with the goal of developing cutting-edge accelerator technologies for a new generation of compact and cost-efficient ion therapy facilities [11]. The primary focus of NIMMS is to advance the use of particles heavier than protons, as proton-based installations are already commercially available. In this context, on the NIMMS initiative, a helium linac developed by the author serves as an injector for a therapy synchrotron and, in parallel, for radioisotope production. The layout of the NIMMS linac is shown in Fig. 2.6.

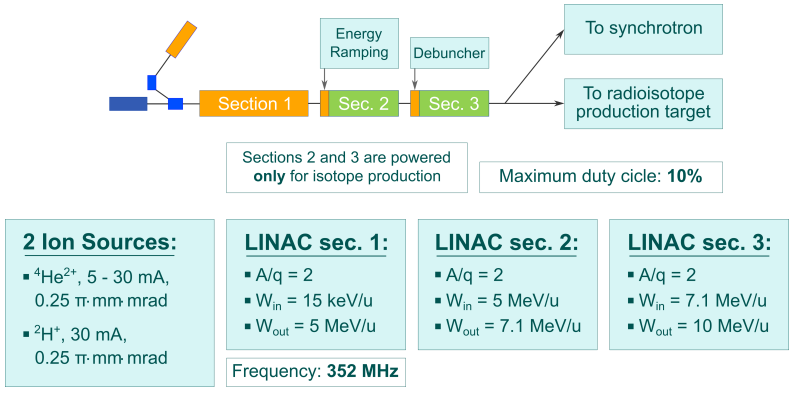


Fig. 2.6. Layout of the NIMMS linac.

The NIMMS linac is powered by one of two available ion sources, providing either helium ions or deuterons. Similar to the HITRI*plus* linac, the ion source is followed by three accelerating

sections. All three sections are capable of accelerating both types of particles provided by the ion sources. The first section accelerates the ions to an energy of 5 MeV/u, which is used either for helium injection into a therapy synchrotron or for radioisotope production with helium ions or deuterons, depending on the demand. The next two sections are also capable of accelerating both helium ions and deuterons but are dedicated solely to radioisotope production. The second section accelerates both ions up to 7.1 MeV/u, while the final section accelerates them to 10 MeV/u. To maximize radioisotope production, the linac must achieve acceleration of both helium ions and deuterons, each with a nominal beam current of 30 mA with 100% beam transmission. The NIMMS linac designed by the author is adapted as a helium injector for the future Advanced Particle Therapy Center for the Baltic States [12].

2.3 Radioisotope production with linac

The linac structures proposed in this Thesis can produce radioisotopes with helium ions or deuterons for diagnostic and therapeutic purposes, depending on market demand. The linac configuration for radioisotope production is shown in Fig. 2.7.

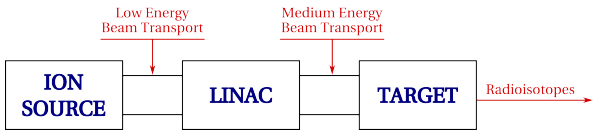


Fig. 2.7. Schematic representation of the linac configuration for radioisotope production.

The International Atomic Energy Agency (IAEA) has compiled a list of several dozen radioisotopes used as tracers in the physical and biological sciences [13]. A list of promising radioisotopes for use in diagnostics and therapeutics, extracted from [13], which can be produced by the linac accelerating helium ions and/or deuterons, is presented in Table 2.1.

The reputable U.S.-based company NUSANO, known for its expertise in radioisotope production, has provided a list of radioisotopes currently in high demand, some of which are shown in Table 2.1 [26]. From Table 2.1, PET (Positron Emission Tomography) produces high-quality three-dimensional images, while SPECT (Single Photon Emission Computed Tomography) generates a series of two-dimensional projections that are used to reconstruct three-dimensional images [27, 28].

On the other hand, radioisotopes that decay by beta-particle emission (used in β^- Therapy), alpha-particle emission (used in Targeted Alpha Therapy – TAT), and electron capture, leading to the emission of Auger electrons (used in Auger Electron-based Radioisotope Therapy – AERT), are suitable for radioisotope therapy (therapeutics) due to their short range in tissue [29]. Additionally, radioisotopes that decay via low-energy gamma photon emission can be employed in brachytherapy, a method involving the physical implantation of isotopes.

Table 2.1. List of prospective radioisotopes for use in diagnostics and therapeutics, producible using a linac that accelerates helium ions and/or deuterons

Radio-isotope	Half-time	Use	Production reaction	Suitable linac energy [MeV/u]	Refer-ences
^{18}F	109.8 min	PET	^{16}O(α, p)^{18}F ^{20}Ne(d, α)^{18}F	10 5	[14] [15]
^{64}Cu	12.7 h	β^- therapy AERT PET	^{64}Ni(d, 2n)^{64}Cu	7.1	[16]
^{67}Cu	61.8 h	$\beta-$ therapy SPET	^{64}Ni(α, p)^{67}Cu	5	[17]
^{68}Ge	270.9 d	*Generator for* ^{68}Ga - PET	^{66}Zn(α, 2n)^{68}Ge	7.1	[18]
^{89}Zr	78.4 h	PET	^{89}Y(d, 2n)^{89}Zr	7.1	[19]
^{103}Pd	17 d	AERT Brachytherapy	^{103}Rh(d, 2n)^{103}Pd	7.1	[20]
^{123}I	13.2 h	SPECT	^{121}Sb(α, 2n)^{123}I ^{122}Te(d, n)^{123}I	7.1 5	[21] [22]
^{177}Lu	6.6 d	β^- therapy	^{176}Yb(d, n)^{177}Lu	5	[23]
^{211}At	7.2 h	TAT SPECT	^{209}Bi(α, 2n)^{211}At	7.1	[24, 25]

Courtesy of K. Paļskis

3. RF and Beam Optics Theory of Linac Structures

In this chapter, the physics behind electromagnetic waves, the behavior of the beam inside linac structures, the software used for complex simulations, and the linac economics are presented. The chapter consists of four sections, each dedicated to a corresponding topic. The first section explains the fundamental concepts necessary for understanding electromagnetic wave properties within the linac structure. The second section focuses on beam behavior during acceleration inside linac structures, providing the necessary expressions for its visualization. The third section describes the developed structures that are presented in this Thesis, applying the theoretical framework established in the first two sections of this chapter. Lastly, the fourth section focuses on the linac economics of Alvarez-type structures used for the acceleration of low-velocity ions.

3.1 Electromagnetic field theory for linac structures

In the interest of designing any linac structure ready for manufacturing, the physics of electromagnetic (EM) wave propagation and its influence on the beam must first be understood. To understand EM modes within a linac structure, we first consider a cylindrical waveguide. When an external EM field is applied to the cylindrical waveguide, the EM waves can have only electric or magnetic components in the direction of wave propagation (longitudinal plane), but not both at the same time. An EM wave in which the electric field is entirely perpendicular to the direction of propagation is known as a Transverse Electric (TE) mode, whereas a wave in which the magnetic field is entirely perpendicular to the direction of propagation is called a Transverse Magnetic (TM) mode. Both TE and TM modes can exist at certain discrete frequencies, dictated by the geometry of the waveguide. By enclosing both ends of the cylindrical waveguide, it becomes a cylindrical resonator in which standing waves are established at specific resonant frequency [30].

The three most commonly used modes in the field of linac accelerators are TM_{010}, TE_{110}, and TE_{210}, with their representations in the cylindrical waveguide shown in Fig. 3.1.

In addition to Fig. 3.1, the cross-section of the cylindrical resonator showing the magnetic field distribution of TM_{01p} and the electric field distribution of TE_{11p} and TE_{21p} family modes is shown in Fig. 3.2.

To achieve a more efficient energy transfer from the external EM field to the beam, drift

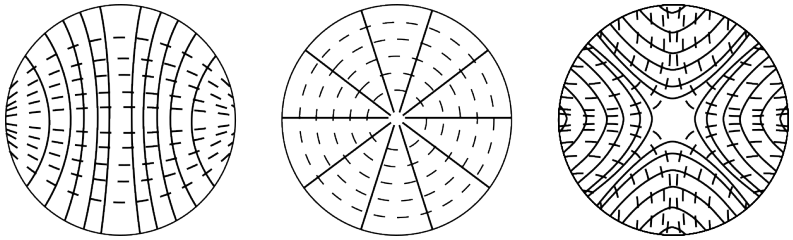


Fig. 3.1. Field configuration of (left) TE_{11}, (middle) TM_{01}, and (right) TE_{21} modes within a cylindrical waveguide (adapted from [31]).

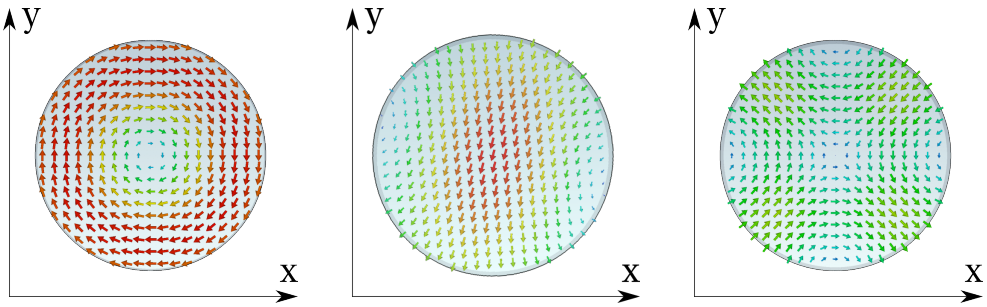


Fig. 3.2. (a) Magnetic field distribution of TM_{01p} family modes; (b) electric field distribution of TE_{11p} family modes; (c) electric field distribution of TE_{21p} family modes. Simulations were performed on a cylindrical resonator using CST Studio Suite.

tubes are introduced within cylindrical resonators (consult Figs. 2.3 and 2.4). The neighboring drift tubes concentrate the electric field along the trajectory of the particles in the space between them, making acceleration more efficient. At the same time, drift tubes act as a Faraday cage to prevent the deceleration of particles when the established field changes polarity.

A cell of a linac structure usually consists of halves of neighboring drift tubes and the space between them, known as the *gap*. A particle traveling through the gap will experience an electric field, as shown in Fig. 3.3.

An arbitrary particle with electric charge q traveling through the gap will also experience an energy gain given by the *Panofsky equation*:

$$\Delta W = qE_0L_cTcos(\phi), \tag{3.1}$$

where E_0 represents the average axial electric field amplitude, and T (sometimes denoted as T_{gap}) is the *transit-time factor* which is an important but complex parameter, encapsulating a significant amount of physics. Since the electric field on the axis is time-varying, a particle cannot experience the same energy gain as it would in the case of a constant direct current (DC) electric field. The ratio of energy gain in a time-varying RF field to that in a constant DC electric field is known as the transit-time factor.

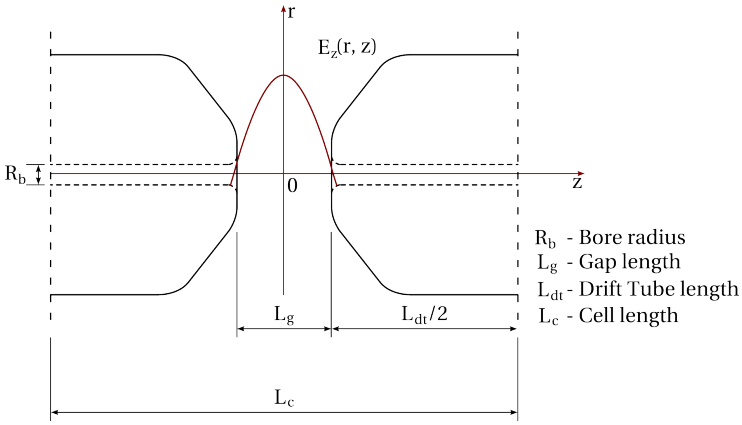


Fig. 3.3. Electric field with a crest in the middle of the gap (adapted from [32])).

The fundamental properties used to characterize any linac structure by providing information about its performance are known as figures of merit, from which the most important is the effective shunt impedance per unit length (Z' or often ZT^2). In most cases during the design process the goal is to maximize the effective shunt impedance per unit length to achieve the highest power efficiency of the structure. The effective shunt impedance per unit length is defined as the ratio between the effective shunt impedance and the length of the resonator:

$$Z' \equiv ZT2 = \frac{Z}{l} = \frac{(V_0 T)^2}{P_d \cdot l} = \frac{(E_0 T)^2}{P_d / l} \tag{3.2}$$

In the case of coupled multi-cell accelerating structures the so-called synchronicity condition must be respected, which simultaneously defines the length of each cell. The synchronicity condition is as follows:

$$L_c = \frac{\beta\lambda}{2\pi}\Delta\phi_c, \tag{3.3}$$

where β is the particle's velocity relative to the speed of light in free space, λ is the RF wavelength, and $\Delta\phi_c$ is the phase shift between two neighboring cells.

For the acceleration of particles, the three most useful (and practical) standing wave (SW) modes are the 0-mode, $\frac{\pi}{2}$-mode, and π-mode due to their accelerating field distribution. The electric field patterns of these three SW modes are shown in Fig. 3.4.

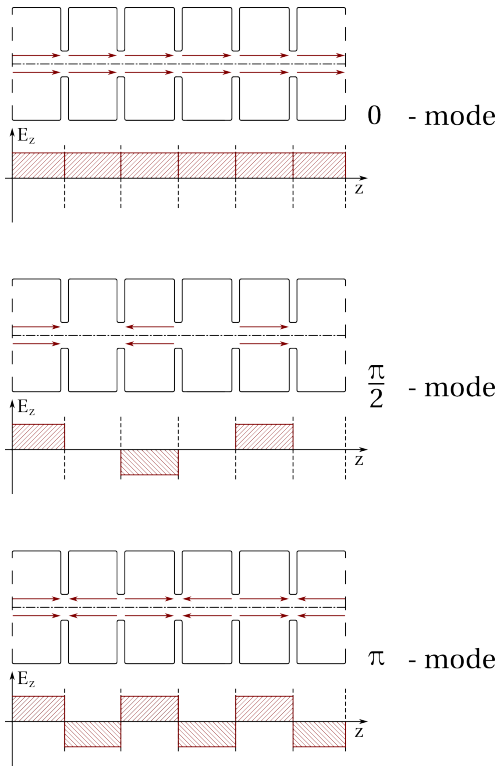


Fig. 3.4. Standing wave modes suitable for particle acceleration in multi-cell coupled cavities (adapted from [33]).

3.2 Beam optics for linac structures

Inside the linac structure, the movement of a particle with charge q and velocity $\vec{v} = (v_x, v_y, v_z)$, after experiencing an external electric field $\vec{E} = (E_x, E_y, E_z)$ and magnetic field $\vec{B} = (B_x, B_y, B_z)$, is described by the Lorentz force (Equation (3.4)):

$$\frac{d\vec{p_r}}{dt} = q\left(\vec{E} + \vec{v} \times \vec{B}\right) \tag{3.4}$$

Once designed, linac structures will optimally accelerate a single particle within a beam of N_p particles. The particle for which the linac structure is designed is called the *synchronous particle*, and it is always in synchronicity with the accelerating field. The phase of the synchronous particle is defined as the synchronous phase (ϕ_s).

Within the linac community, by convention, the accelerating field varies over time as a cosine function, with the crest at the origin ($\phi = 0$) consisting of stable and unstable regions as illustrated in Fig. 3.5. The stable region is the region where the beam clusters around the synchronous particle, while the unstable region is the region that will eventually lead to beam loss.

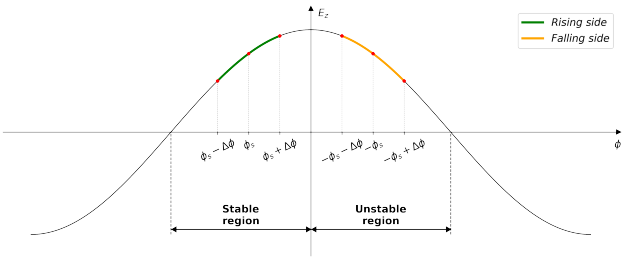


Fig. 3.5. Accelerating field with illustrated stable and unstable regions.

For transverse beam analysis, especially important parameters are the amplitude function, known as the *beta function*, and the constant $\varepsilon_{xx'}$, known as the *beam emittance* in the horizontal phase space, since both are related to the beam's shape and size.

Besides the $\beta(s)$ function, there are two additional functions that are useful in transverse beam analysis, namely the $\alpha(s)$ and $\gamma(s)$ functions, both of which depend on the beam abscissa s. The $\alpha(s)$, $\beta(s)$, and $\gamma(s)$ functions are collectively referred to as the *Courant–Snyder parameters* or simply the *Twiss parameters*. Both the $\alpha(s)$ and $\gamma(s)$ parameters depend on the $\beta(s)$ function, and they are defined as:

$$\alpha(s) = -\frac{1}{2}\frac{d\beta(s)}{ds} \text{ and} \tag{3.5}$$

$$\gamma(s) = \frac{1+\alpha^2(s)}{\beta(s)}. \tag{3.6}$$

According to Eqs. (3.5) and (3.6), both the $\alpha(s)$ and $\gamma(s)$ parameters depend on the $\beta(s)$ function, while the $\beta(s)$ function represents a property of the linac structure. Considering the Twiss parameters, the so-called Courant–Snyder invariant is derived from Hill's equation:

$$\gamma(s)x^2 + 2\alpha(s)xx' + \beta(s)x'^{\,2} = \varepsilon, \tag{3.7}$$

where x represents the position and x' is the angular deviation of the particle in the horizontal plane. Eq. (3.7) represents the general equation of a tilted ellipse, where the angle of rotation (θ_e) depends on the Twiss parameters through the following relation:

$$\tan(2\theta_e) = \frac{4\alpha(s)}{\gamma(s) - \beta(s)} \tag{3.8}$$

It can be easily shown that the area of the ellipse, as expressed in Eq. (3.7), is $A_{xx'} = \pi\varepsilon_{xx'}$, which implies that the area of the Twiss ellipse is proportional to the beam emittance in that plane.

The visual representation of the Twiss ellipse in the horizontal plane, with indicated characteristic points in the horizontal plane, is shown in Fig. 3.6.

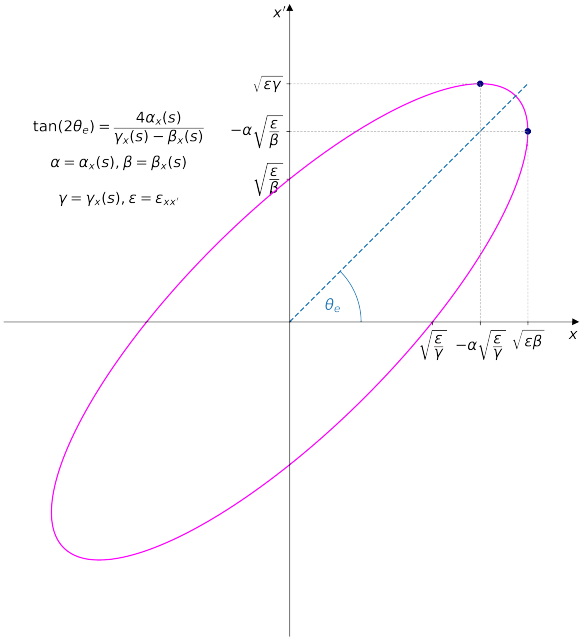


Fig. 3.6. Twiss ellipse in horizontal phase space with characteristic points.

Fig. 3.7 illustrates the beam envelope for both the horizontal plane (teal) and the vertical plane (orange), along with the Twiss ellipses at the center of each element.

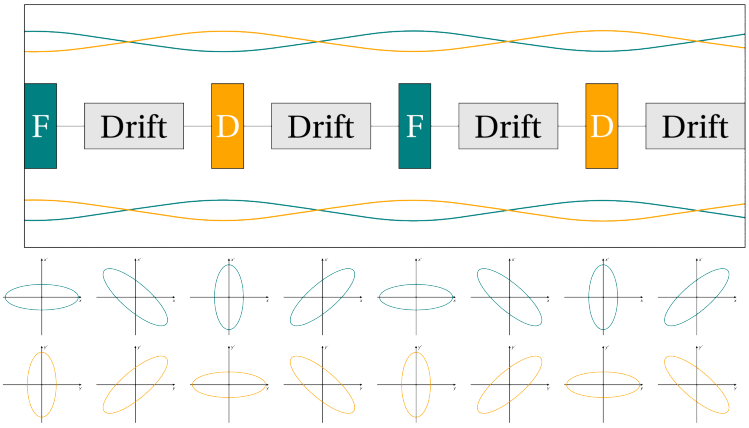


Fig. 3.7. Beam envelope in the horizontal plane (teal) and vertical plane (orange), along with Twiss ellipses plotted at the center of each element.

3.3 Analyzed structures for acceleration and beam manipulation

As a proton linac structure, the DTL has proven to be power-efficient with high shunt impedance up to energies of around 60 MeV, beyond which it is typically replaced by more power-efficient structures, such as the Cell-Coupled Drift Tube Linac (CCDTL) [6]. The DTL operates in the 0-mode. This structure is characterized by the presence of Permanent Magnet Quadrupoles (PMQs) inside each Drift Tube (DT). A section of a single DTL cell is shown in Fig. 3.8 (a), while a single DT is presented in Fig. 3.8 (b).

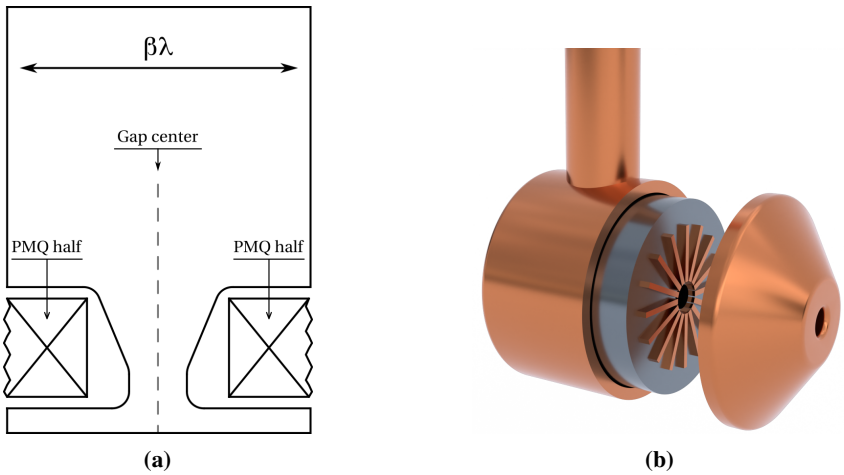


Fig. 3.8. (a) The section of one cell of DTL; (b) a drift tube with PMQ within DTL.

The DTL resonates in TM_{010} electromagnetic mode, which is characterized by a longitudinal electric field and an azimuthal magnetic field, as shown in Figs. 3.1 and 3.2 (a). Regarding transverse beam focusing, DTL structures typically use either FODO or FOFODODO lattices, where F represents a PMQ that focuses the beam in the horizontal direction and defocuses it in the vertical direction, D indicates a PMQ that defocuses the beam in the horizontal direction and focuses it in the vertical direction, and O denotes the drift space between two PMQs located within neighboring drift tubes where the beam is neither focused nor defocused in both the horizontal and vertical planes. The 3D model of the DTL is shown in Fig. 3.9.

A modification of the DTL (the QA-DTL) is required to allow the acceleration of protons and particles heavier than protons at lower energies compared to what is possible with the DTL. The modification made in comparison to the DTL is a reduction in the number and an increase in the length of drift tubes that accommodate PMQs for transverse beam focusing. As with the DTL, the QA-DTL is also a 0-mode structure. Fig. 3.10 shows some QA-DTL configurations compared with the DTL.

The periodicity factor n_p is a very important parameter that directly affects the efficiency of the linac structure, so it needs to be chosen carefully. From the beam dynamics point of view, the

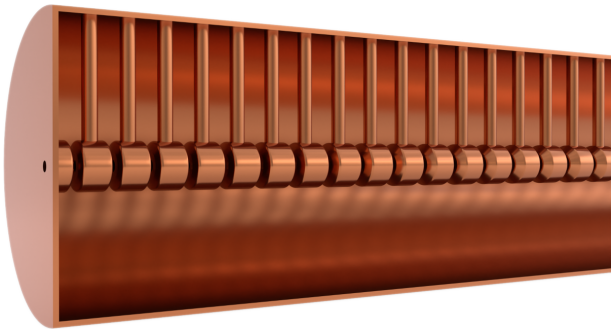


Fig. 3.9. The 3D model of DTL.

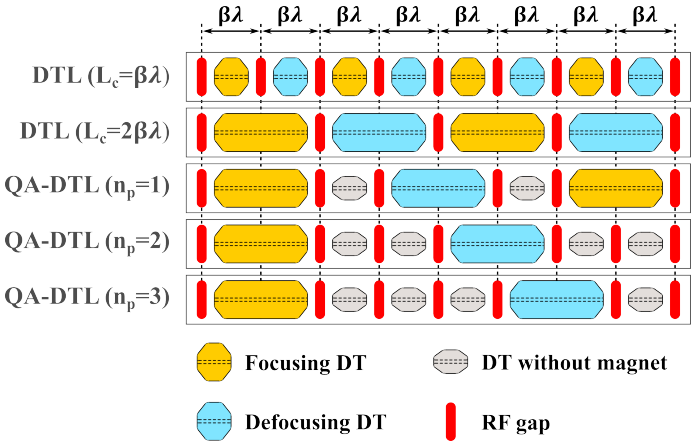


Fig. 3.10. Comparison between different QA-DTL configurations and DTL (adapted from [34]).

periodicity factor is selected as a trade-off between the PMQ gradient and beam transmission. The QA-DTL reaches its highest efficiency when the periodicity factor is two ($n_p = 2$) [34, 35]. In this case, the super-period consists of two drift tubes without PMQs and two halves of drift tubes containing PMQs, as shown in Fig. 3.11.

Similar to the DTL, the QA-DTL also resonates in the TM_{010} electromagnetic mode, which is characterized by a longitudinal electric field and an azimuthal magnetic field, as shown in Figs. 3.1 and 3.2 (a). The 3D model of the QA-DTL segment, featuring a super-period with a periodicity factor of two, is shown in Fig. 3.12.

The most widely used H-mode linac structure, for the acceleration of particles heavier than protons, is the IH-DTL. A variation of the IH-DTL that was proposed, but never built, is the S-IH-DTL. Both linac structures are π-mode structures, and both resonate in the TE_{110} electromagnetic mode, which is characterized by a longitudinal magnetic field and an azimuthal electric field, as shown in Figs. 3.1 and 3.2 (b). One cell of an H-mode linac structure is shown in Fig. 3.13 (a), while one DT of the same structure is presented in Fig. 3.13 (b).

The transverse focusing and defocusing in IH-DTL are achieved using quadrupole doublets,

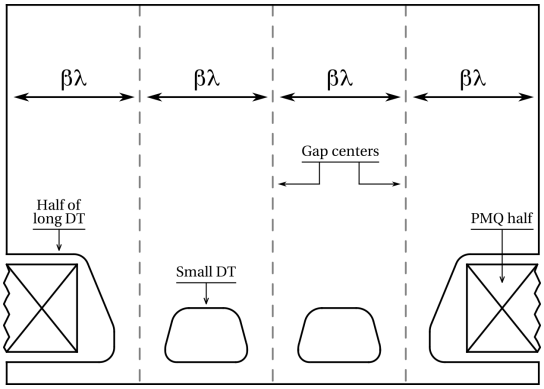


Fig. 3.11. One super-period of QA-DTL with periodicity factor of two.

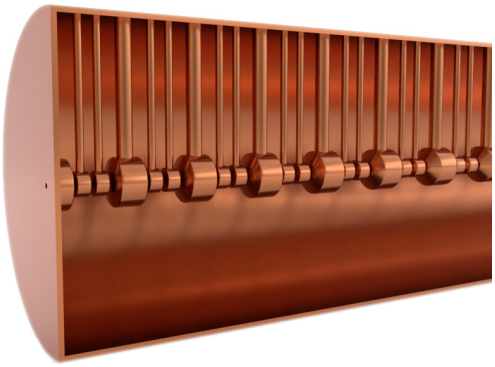


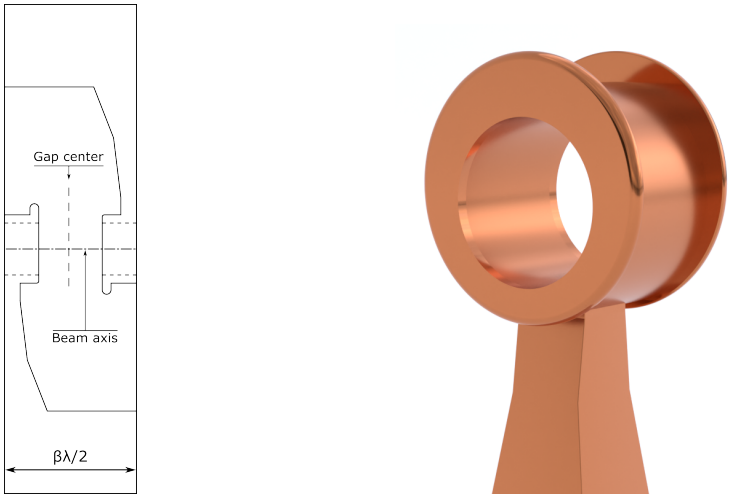
Fig. 3.12. The 3D model of QA-DTL featuring super-periods with the periodicity factor of two.

triplets, or solenoid lenses [36], which are placed after a certain number of cells, as shown in Fig. 3.14. The main difference between IH-DTL and S-IH-DTL is the placement of quadrupoles – in the case of S-IH-DTL, the quadrupoles are located outside the accelerating structure, with two neighboring cavities surrounding them.

For more efficient beam injection into a synchrotron, an additional RF structure known as a *debunching cavity* (DEB) is required. The primary goal of the DEB is to reduce energy spread as much as possible. Through the drift space, the beam expands in the longitudinal phase space, resulting in an elongated and narrowed Twiss ellipse. During DEB operation, the EM field within the structure is excited in such a way that the zero-crossing phase from Fig. 3.5 is positioned at the center of the cell gap. The interaction between the EM field (and thus the voltage) and the beam results in beam rotation in the longitudinal phase space, as illustrated in Fig. 3.15.

The angle of beam rotation depends on the EM field amplitude, which directly corresponds to the voltage applied to the cavity. A stronger voltage amplitude will lead to a stronger beam rotation in longitudinal phase space. The main goal of the DEB is to rotate the beam in longitudinal phase space until it is horizontally positioned.

On the other hand, the Energy Ramping Cavity (ERC) is not as critical as the DEB and can



(a) **(b)**

Fig. 3.13. (a) The 2D schematic of one cell of H-mode cavity; (b) a drift tube within H-mode drift tube linac.

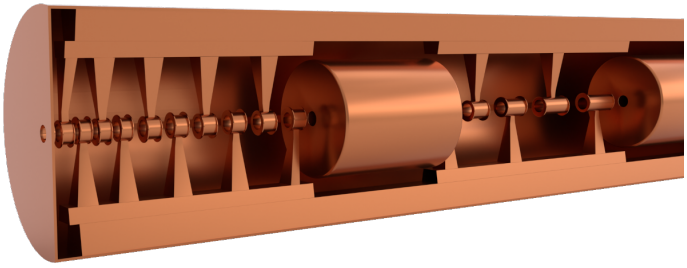


Fig. 3.14. The 3D model of IH-DTL.

be omitted from the linac configuration. The goal of the ERC is to slightly ramp the energy of each beam bunch. To achieve this energy displacement, the EM field is excited in such a way that its phase constantly oscillates between $\varphi_0 - \Delta\varphi$ and $\varphi_0 + \Delta\varphi$, ensuring that each successive beam bunch experiences the desired phase, as illustrated in Fig. 3.16.

For better visualization, the beam bunches with extreme energy displacements (those with the highest and lowest energy values), along with the beam bunch that remains unaffected by the ERC, are shown in Fig. 3.17.

Both DEB and ERC share a similar geometry, with slight differences in gap size and/or cell length. Different types of single-cell DEB and ERC are shown in Fig. 3.18.

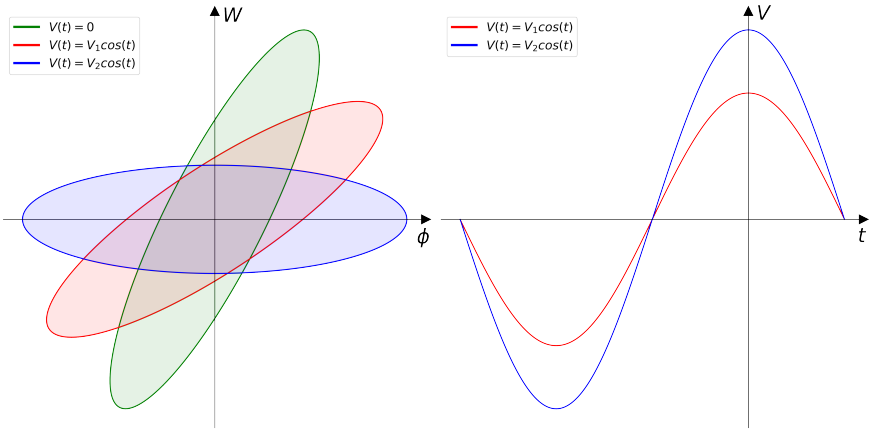


Fig. 3.15. (Left) Twiss ellipses within the DEB in the presence of voltage with different amplitudes; (right) the voltage with different amplitudes corresponding to the ellipses on the left. The green Twiss ellipse occurs when the DEB is not in operation.

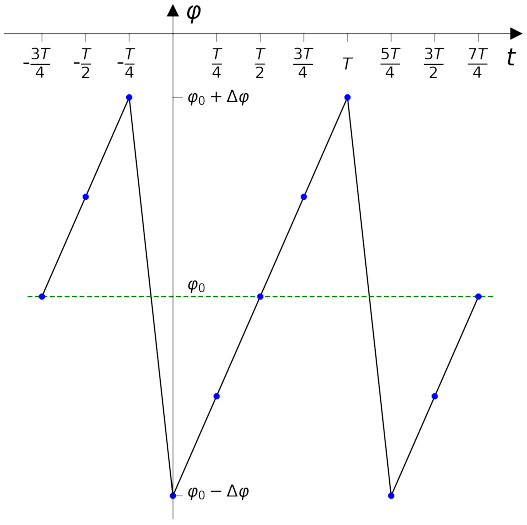


Fig. 3.16. Phase oscillation within the ERC; φ_0 corresponds to the zero-crossing phase. The blue points represent the phase at the center of the gap for each upcoming beam bunch.

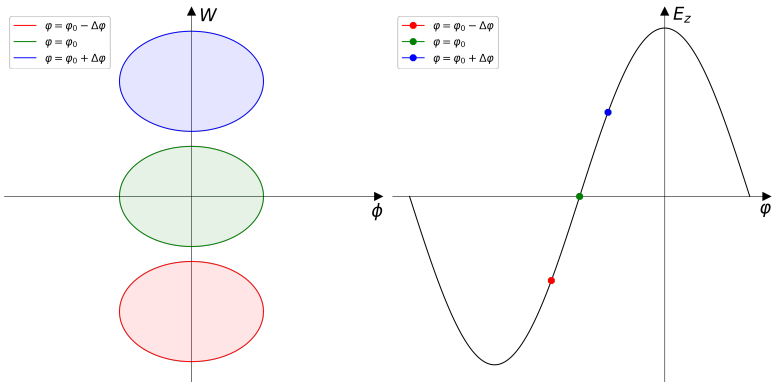
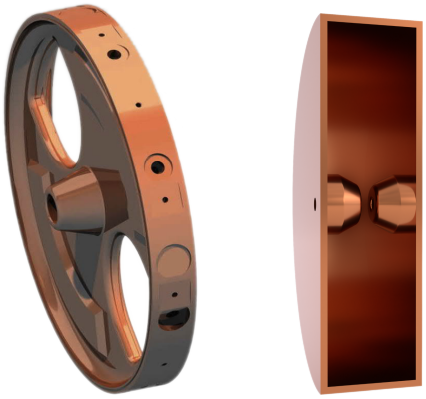


Fig. 3.17. (Left) Twiss ellipse within the ERC in the presence of an external EM field with different phases in the middle of the gap; (right) the external EM field corresponding to the ellipses on the left.



(a) **(b)**

Fig. 3.18. (a) π-mode structure and (b) 0-mode structure used as DEB or ERC units.

3.4 Cost efficiency of Alvarez-type linac structures

One of the key factors influencing the selection of an accelerating structure is the cost of the RF system and the cost of the accelerating structure, collectively referred to as the total cost (C_{tot}), which can be expressed as follows [32]:

$$C_{tot} = lC_l + (P_d + P_b)C_p \simeq lC_l + P_d C_p, \tag{3.9}$$

where C_p is the capital cost of the radio-frequency system, C_l is the capital cost of the accelerating structure, l is the length of the cavity, P_b is the beam power, and P_d is the power dissipation in the cavity. Furthermore, by rearranging Eq. (3.9) the following is obtained:

$$C_{tot} = \frac{\Delta W}{q}\left(\frac{C_l}{(E_0T)} + \frac{(E_0T)C_p}{ZT^2}\right) \tag{3.10}$$

Differentiating Eq. (3.10) with respect to E_0T and then equating it to zero, the condition of minimum cost is obtained:

$$C_p = \frac{ZT^2}{(E_0T)^2}C_l \tag{3.11}$$

According to Eq. (3.10), there is only one value of accelerating field (E_0T) at which the total cost of the structure is minimal, as shown in Fig. 3.19.

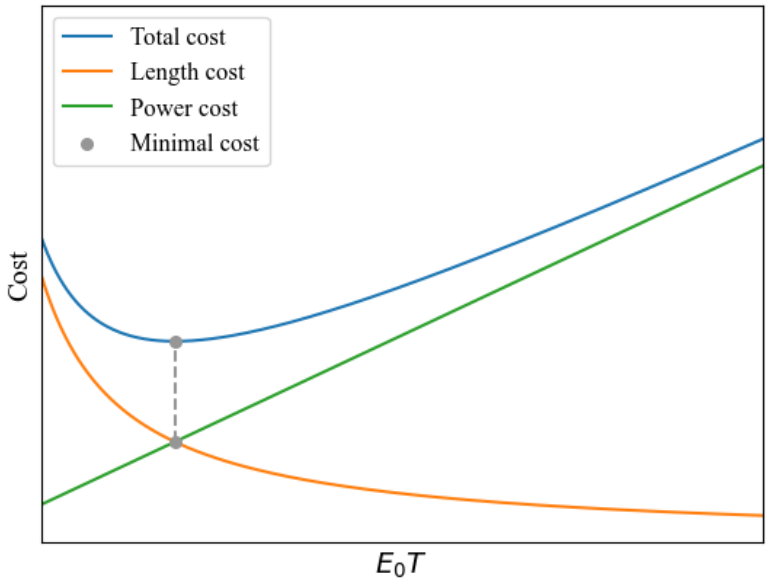


Fig. 3.19. Total cost of the structure as the function of the accelerating field, with the emphasis on the minimal cost.

Furthermore, substituting Eq. (3.11) into Eq. (3.9), the total cost can be related to the cavity

cost per unit length (C_l):

$$C_{tot} = \left(l + \frac{P_d Z T^2}{(\frac{\Delta W}{ql})^2} \right) C_l \tag{3.12}$$

The cost of the tank and the cost of the permanent magnet were estimated to scale relative to the cost of the drift tube as follows:

$$C'_{tank} \simeq 5.1 C'_{dt}, \tag{3.13}$$

$$C'_{pmq} \simeq 0.2 C'_{dt}. \tag{3.14}$$

The ratio of costs provided by Eqs. (3.13) and (3.14) is coherent with the costs of LINAC4, the linear accelerator currently operating at CERN [6].

Further simplification, with detailed derivation provided in the Thesis, leads to the capital cost of conventional DTL and QA-DTL:

$$C_l^{DTL} = \frac{(5.1l + 1.2N_{cell})}{l} C'_{dt}, \tag{3.15}$$

$$C_l^{QA} = \frac{(5.1l + 0.8N_{cell})}{l} C'_{dt}. \tag{3.16}$$

All necessary data from both studies have been summarized in Table 3.1.

Table 3.1. List of data regarding conventional DTL and QA-DTL

	DTL	**QA-DTL**	**Units**
l	6.4	4.65	m
P_d	1077.3	570	kW
ZT^2	31.5	67.7	MΩ/m
ΔW	48	48	MeV
q	4	4	-
N_{cell}	104	57	-

A comparison of the calculated total costs (Eq. (3.12)) reveals that the total cost of QA-DTL is 61% lower than that of conventional DTL, making it a more cost-effective option for low-energy ion acceleration applications.

4. Mathematical Model for Optimizing Geometry Parameters of Linac Structures

The RF designs of both DTL and QA-DTL were carried out using Poisson/SUPERFISH codes, a 2D EM simulation software developed at Los Alamos National Lab (LANL) [37]. Poisson/SUPERFISH was selected since it has been benchmarked against most of the linac structures currently in operation. Poisson/SUPERFISH is a suite of programs designed for the computation of magnetostatic and electrostatic fields, and for simulating the field distribution within accelerating structures in a 2D Cartesian system [38].

4.1 Simulation software

In the case of 3D EM simulation software, *CST Studio Suite* was used due to its versatility, high accuracy in solving Maxwell's equations, and its eigenmode solver, particularly suited for high-frequency linac structure design [39].

The beam dynamics simulations were performed using TraceWin codes due to their capability to simulate complex beamline configurations, accurately account for space charge effects, and provide detailed insights into particle trajectories, phase space evolution, and beam losses. In addition, they offer powerful optimization tools to enhance accelerator performance and minimize emittance growth [40].

Two Graphical User Interfaces (GUIs) were developed by the author using the programming language C#. One of the developed GUIs, called A-GUI, is used for optimizing DTL structures by maximizing effective shunt impedance per unit length (ZT^2), while the other, named QA-GUI, is specifically designed for the optimization of QA-DTL cavities, also maximizing ZT^2. The interface of A-GUI is shown in Fig. 4.1.

The second developed GUI (QA-GUI) is considerably more complex than A-GUI. It facilitates the optimization of QA-DTL super-periods, which can be divided into three independent sub-cells. The interface of QA-GUI is shown in Fig. 4.2.

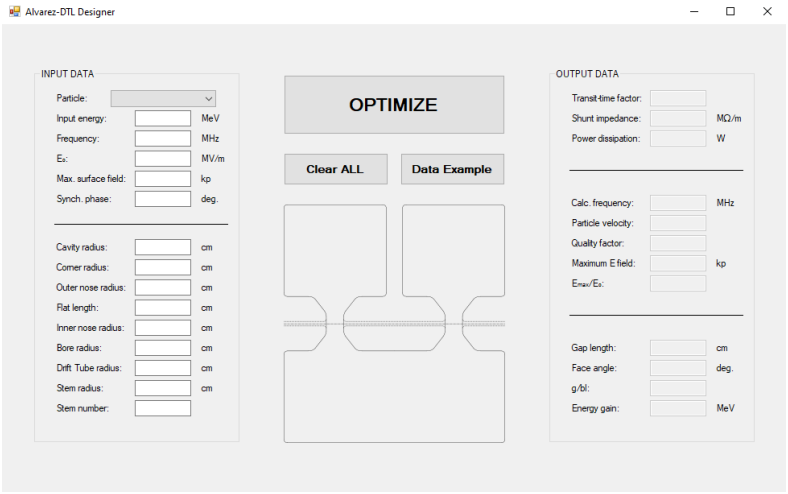


Fig. 4.1. Interface of A-GUI used for optimization of DTL cells.

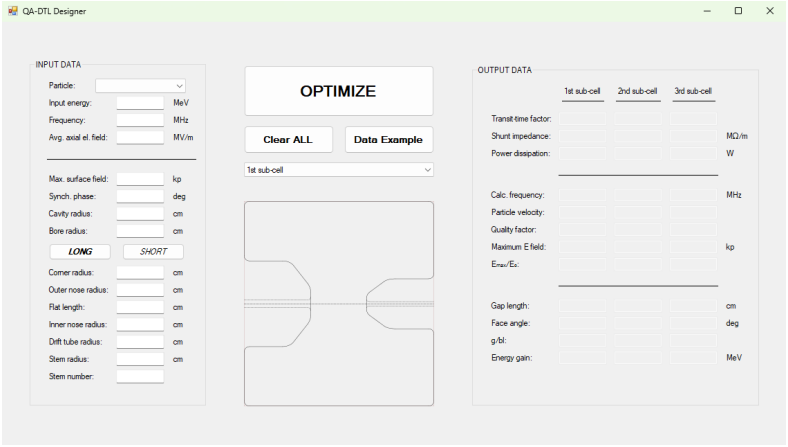


Fig. 4.2. Interface of QA-GUI used for the optimization of QA-DTL super-periods.

4.2 Design procedures and optimization algorithms

As long as the chosen linac structure is of the Alvarez type, the RF design process remains generally the same. During the design process, several constraints must be respected:

1. Every DT within the DTL, or every long DT within the QA-DTL, must be long enough to accommodate the quadrupole magnet.

2. The maximum electric field within the linac structure must not exceed the defined Kilpatrick limit in order to prevent potential electrical breakdowns.

3. The bore radius must be large enough to prevent beam interaction with the DT walls, thus

avoiding unnecessary beam losses.

4. Every cell must resonate at the desired resonant frequency.

To meet all the aforementioned constraints, the geometry parameters shown in Fig. 4.3 must be carefully selected for each cell during the design process.

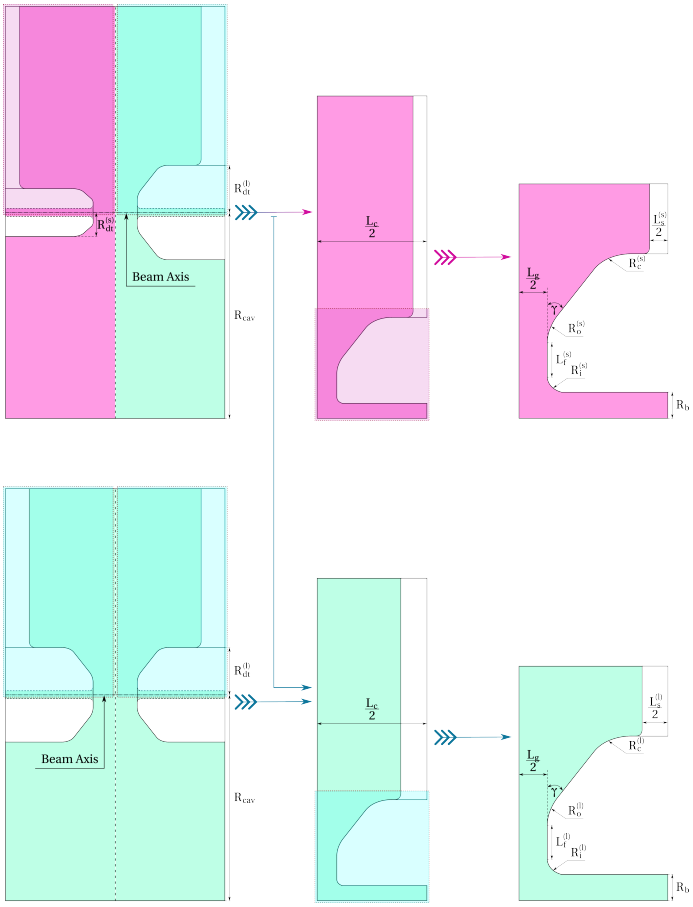


Fig. 4.3. (Top) First or last sub-cell of QA-DTL super-period; (bottom) middle sub-cell of QA-DTL super-period or cell of DTL; with geometry parameters: L_s – stem diameter, L_g – gap length, L_c – cell length, R_{cav} – cavity radius, R_{dt} – drift tube radius, R_c – corner radius, γ – face angle, R_o – outer nose radius, L_f – flat edge length, R_i – inner nose radius, R_b – bore radius (adapted from [41]). Index s exists only in QA-DTL and denotes the shorter DT, while the index l exists in both QA-DTL (for the longer DT) and DTL (for every DT).

The algorithm outlining the complete procedure for designing DTL and QA-DTL from start to finish is presented in Fig. 4.4.

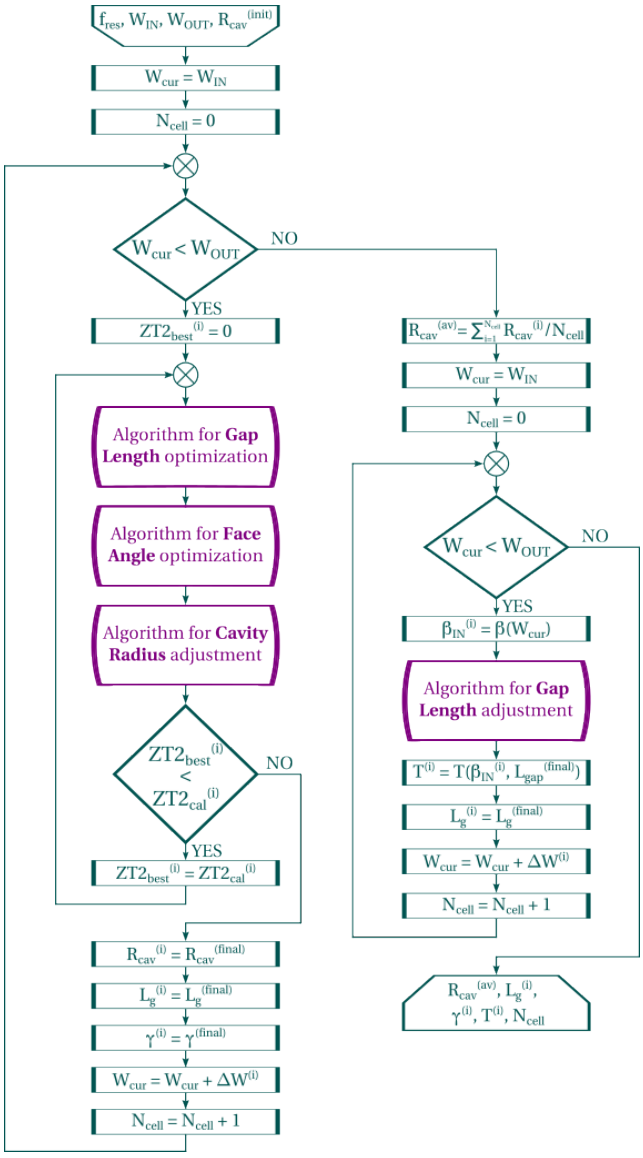


Fig. 4.4. Algorithm for designing the most optimal DTL and QA-DTL for the highest effective shunt impedance per unit length.

Due to the complexity of the geometry, the RF design of the IH-DTL cannot be performed with 2D EM simulation software such as Poisson/SUPERFISH codes. Instead, more sophisticated 3D EM software, such as CST Studio Suite, must be used.

The complete procedure for designing IH-DTL has been developed, as shown in Fig. 4.5.

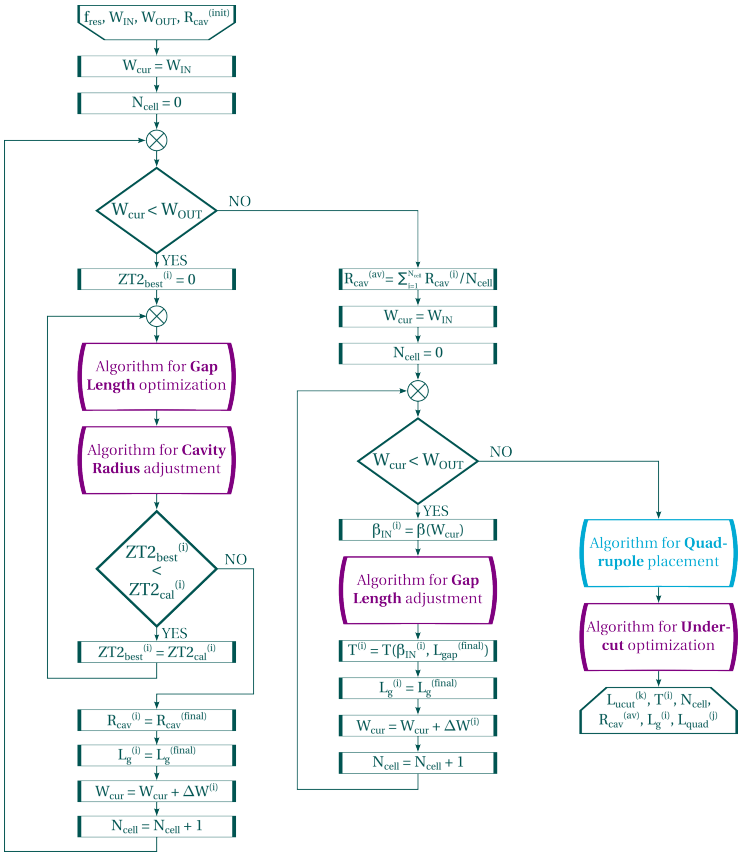


Fig. 4.5. Algorithm for designing the IH-DTL for the highest effective shunt impedance per unit length.

5. Research Results

In this chapter, the obtained results are shown, detailing the design, analysis, and comparison of various linac structures developed for three different applications.

The first application aims to design a linac for carbon ions, as required by the HITRI*plus* project. This linac configuration operates as a synchrotron injector for carbon ion therapy. The second application is dedicated to the development of a linac for helium ions, as required by the NIMMS study at CERN. This linac will serve as a synchrotron injector for helium cancer therapy and, at the same time, for the production of radioisotopes. For the third application, the design of a linac structure developed exclusively for radioisotope production is presented, without the capability to operate as a synchrotron injector.

5.1 HITRI*plus* carbon linac designs

The HITRI*plus* linac consists of three sections. For the first section, the QA-DTL was chosen, designed to accelerate carbon ions from 0.7 MeV/u to 5 MeV/u. The second and third sections are composed of two DTL structures, designed to further accelerate helium ions from 5 MeV/u to 7.1 MeV/u, and then from 7.1 MeV/u to 10 MeV/u, respectively.

5.1.1 Quasi-Alvarez Drift Tube Linac for carbon injection into synchrotron

The RF design of the QA-DTL for accelerating carbon ions from 0.7 MeV/u to 5 MeV/u was performed using the Poisson/SUPERFISH codes. The electric field distributions are shown in Fig. 5.1.

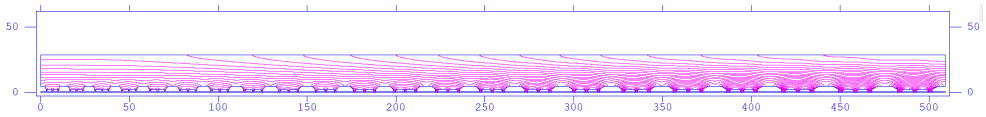


Fig. 5.1. Electric field distribution in QA-DTL for carbon ion acceleration from 0.7 MeV/u to 5 MeV/u, simulated with Poisson/SUPERFISH codes.

The developed QA-DTL operates at a frequency of 352.2 MHz. The RF and geometry parameters of the QA-DTL are summarized in Table 5.1, while the beam dynamics parameters are listed in Table 5.2.

Table 5.1. RF and geometry parameters of the QA-DTL for carbon ion acceleration from 0.7 MeV/u to 5 MeV/u.

	C-ions	He-ions	Units
Operating frequency	352.2		MHz
Input energy	8.4	2.8	MeV
Output energy	60	20	MeV
Peak beam current	0.6	5	mA
Accelerating field	3.5	2.3	MV/m
Synchronous phase	–35 to –24		deg
Length	5.1		m
No. of super-periods	22		-
Effective shunt impedance	67.68		MΩ/m
Power dissipation	626	280	kW

Table 5.2. Beam parameters of the QA-DTL for carbon ion acceleration from 0.7 MeV/u to 5 MeV/u

	C-ions	He-ions	Units
Bore radius	7.5		mm
Input tran. norm. emittance (rms)(xx')	0.250	0.300	π.mm.mrad
Input tran. norm. emittance (rms)(yy')	0.250	0.300	π.mm.mrad
Output tran. norm. emittance (rms)(xx')	0.299	0.317	π.mm.mrad
Output tran. norm. emittance (rms)(yy')	0.278	0.351	π.mm.mrad
Input long. norm. emittance (rms)	1.191	0.473	π.deg.MeV
Output long. norm. emittance (rms)	1.215	0.613	π.deg.MeV
Energy spread (for 2σ (95% beam))	$\pm$0.77	$\pm$1.49	%
Transmission	100	100	%

The transverse and longitudinal beam envelopes from the entrance of the QA-DTL (at 0.7 MeV/u) to its exit (at 5 MeV/u) are shown in Fig. 5.2 for carbon ions at a nominal beam current of 0.6 mA. These envelopes provide valuable insight into the beam's evolution through

the linac. To make the graphs compact and comparable, both transverse planes are plotted on one graph, with the envelope in the horizontal plane represented by the red line, and the envelope in the vertical plane highlighted by the blue line.

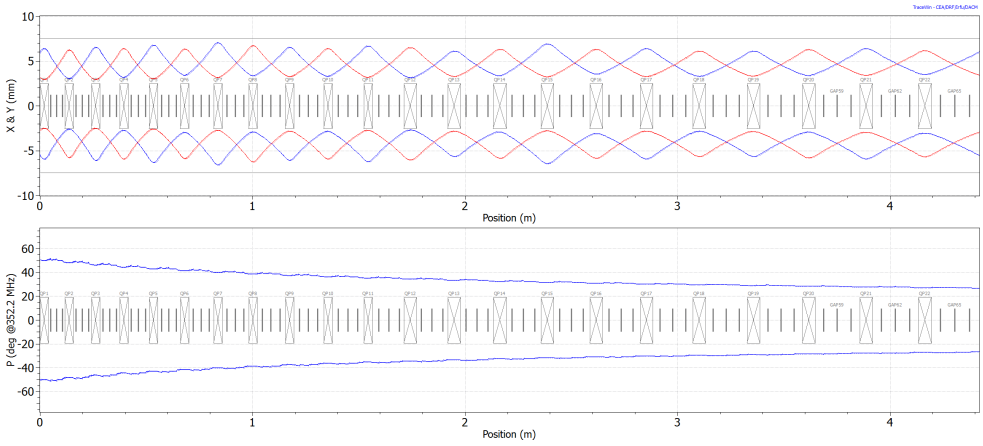
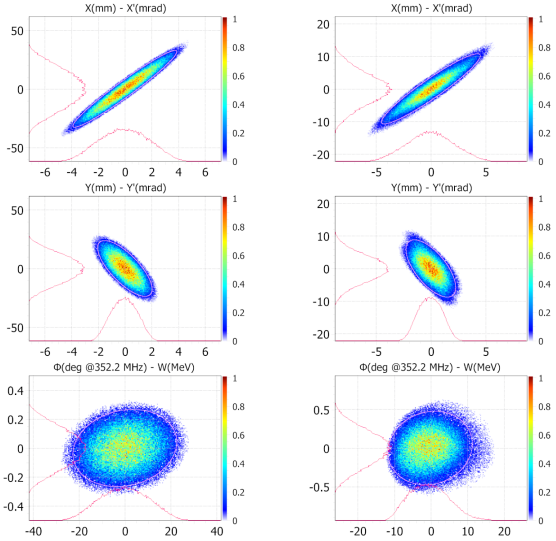


Fig. 5.2. Beam envelopes along the QA-DTL from 0.7 MeV/u to 5 MeV/u for (a) carbon ions and (b) helium ions. For each accelerated ion, the top plot represents transverse beam envelopes in the xz and yz planes, while the bottom plot shows the phase envelope.

The phase spaces showing the beam of carbon ions in the transverse and longitudinal planes at the entrance and exit of the QA-DTL are presented in Fig. 5.3.



(a) **(b)**

Fig. 5.3. Carbon ion phase space (left column) at 0.7 MeV/u and (right column) at 5 MeV/u with the nominal beam current of 0.6 mA within QA-DTL.

5.1.2 Alvarez Drift Tube Linac for radioisotope production

To extend the acceleration of helium ions up to 10 MeV/u in the HITRI*plus* design, the first section is followed by two separate Drift Tube Linacs (DTL cavities) that are powered only when radioisotopes are produced. When the beam is injected into the synchrotron, both DTL cavities are off. The design uses two DTL structures instead of one to allow for the radioisotope production with helium ions at two different energies. When the first DTL is in operation and the second is off, the helium ions reach an energy of 7.1 MeV/u, the optimal value for producing one of the most promising alpha-emitting radioisotopes for cancer treatment, 211-Astatine [10]. In the case where both DTL structures are in operation, the helium ions are accelerated to an energy of 10 MeV/u and then used for the production of commonly demanded radioisotopes, such as 18-Fluorine, the most widely used radiotracer in PET (Positron Emission Tomography) imaging for early detection of tumors [42].

The RF design of both DTL structures was carried out with the Poisson/SUPERFISH codes. The first DTL is referred to as DTL1, while the second DTL is denoted as DTL2. Electric field distributions inside both DTL1 and DTL2 are shown in Fig. 5.4.

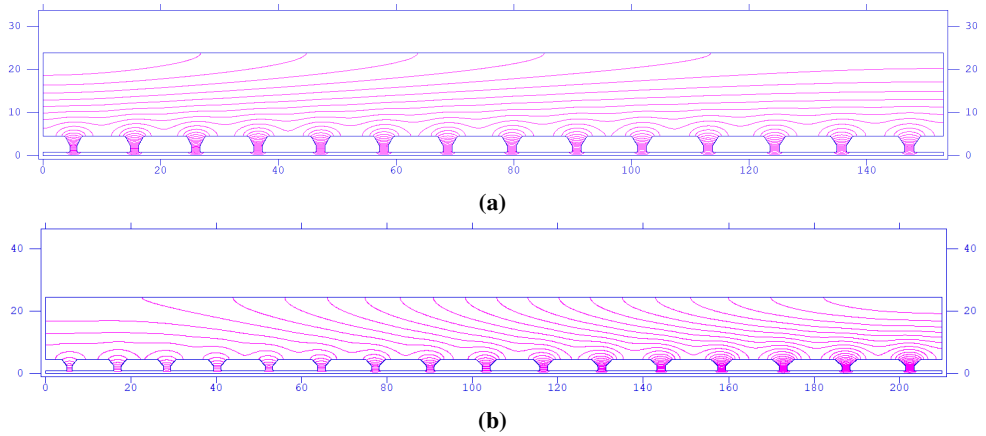


Fig. 5.4. Electric field distribution in (a) DTL1, and (b) DTL2, for acceleration of 5 mA helium ions from (a) 5 MeV/u to 7.1 MeV/u, and (b) 7.1 MeV/u to 10 MeV/u, respectively, simulated with Poisson/SUPERFISH codes.

The RF and geometry parameters for DTL1 and DTL2, designed for the acceleration of helium ions from 5 MeV/u to 10 MeV/u, are summarized in Table 5.3.

Table 5.3. RF and geometry parameters of the DTL1 and DTL2 for acceleration of 5 mA helium ions from 5 MeV/u to 10 MeV/u

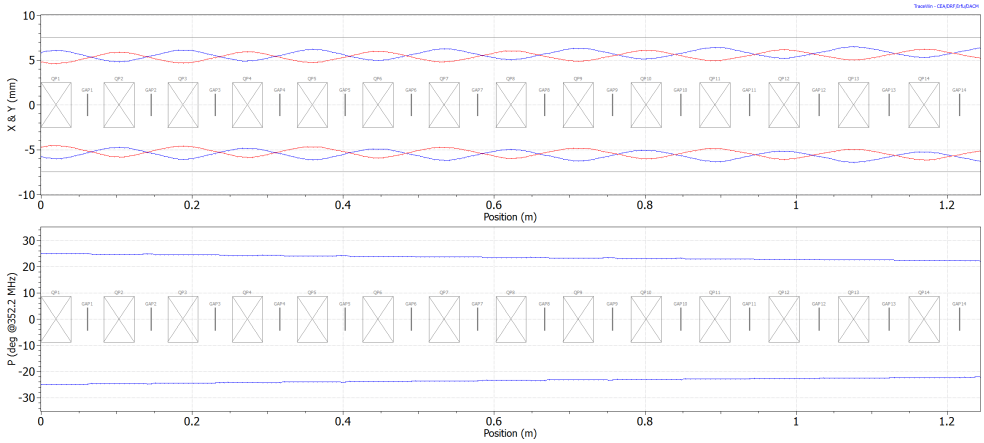
	DTL1	**DTL2**	**Units**
Operating frequency	352.2		MHz
Input energy	20	28.4	MeV
Output energy	28.4	40	MeV
Peak beam current	5		mA
Accelerated field	3.1		MV/m
Synchronous phase	–24		deg
Length	1.53	2.09	m
No. of cells	14	16	-
Effective shunt impedance	66.77	67.53	MΩ/m
Power dissipation	181	253	kW

The beam parameters for DTL1 and DTL2, designed to accelerate 5 mA helium ions from 5 MeV/u to 7.1 MeV/u and from 7.1 MeV/u to 10 MeV/u, respectively, are summarized in Table 5.4.

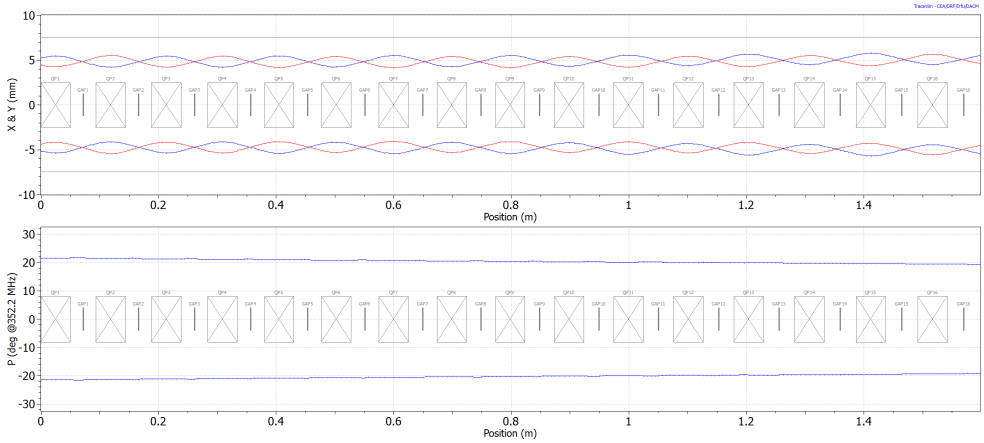
Table 5.4. Beam parameters of the DTL1 and DTL2 for acceleration of 5 mA helium ions from 5 MeV/u to 10 MeV/u

	DTL1	**DTL2**	**Units**
Bore radius	7.5		mm
Input tran. norm. emittance (rms)(xx')	0.317	0.317	π.mm.mrad
Input tran. norm. emittance (rms)(yy')	0.351	0.351	π.mm.mrad
Output tran. norm. emittance (rms)(xx')	0.317	0.317	π.mm.mrad
Output tran. norm. emittance (rms)(yy')	0.351	0.351	π.mm.mrad
Input long. norm. emittance (rms)	0.613	0.629	π.deg.MeV
Output long. norm. emittance (rms)	0.629	0.633	π.deg.MeV
Energy spread (for 2σ (95% beam))	$\pm$1.12	$\pm$0.89	%
Transmission	100	100	%

Fig. 5.5 illustrates the transverse and longitudinal beam envelopes as helium ions travel through DTL1 and DTL2. The envelopes are shown from the entrance of DTL1 at 5 MeV/u to its exit at 7.1 MeV/u, and from the entrance of DTL2 at 7.1 MeV/u to its exit at 10 MeV/u, with a nominal beam current of 5 mA.



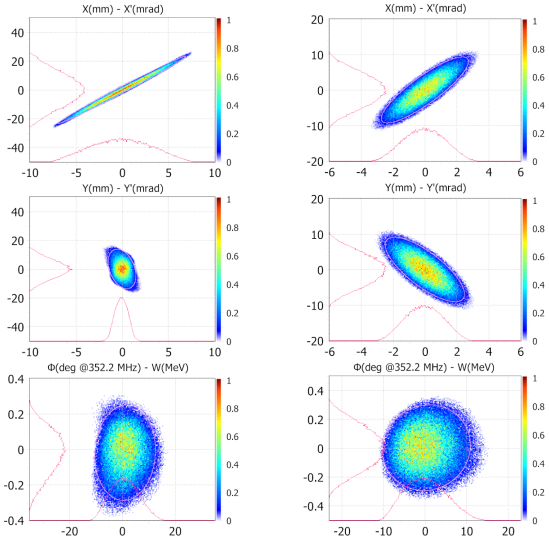
(a)



(b)

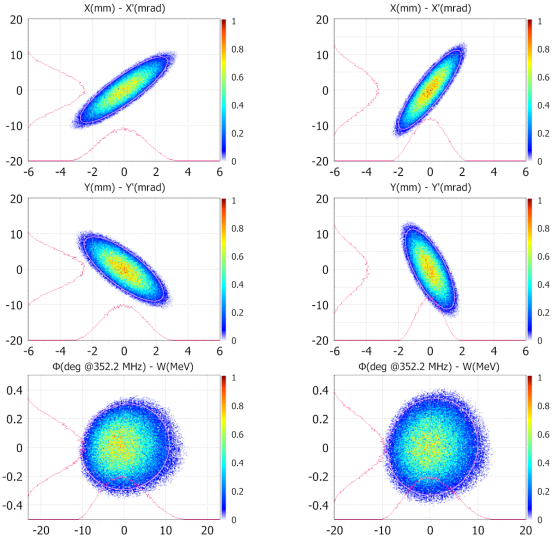
Fig. 5.5. Beam envelopes along the (a) DTL1 from 5 MeV/u to 7.1 MeV/u and (b) DTL2 from 7.1 MeV/u to 10 MeV/u for helium ions. For each structure, the top plot represents transverse beam envelopes in the xz and yz planes, while the bottom plot shows the phase envelope.

Meanwhile, the phase spaces of 10^5 helium ions in both transverse and longitudinal planes at the input and output energies of DTL1 are presented in Fig. 5.6, while those at the entrance and exit of DTL2 are shown in Fig. 5.7.



(a) **(b)**

Fig. 5.6. Helium ion phase space (left column) at 5 MeV/u and (right column) at 7.1 MeV/u with the nominal beam current of 5 mA within DTL1.



(a) **(b)**

Fig. 5.7. Helium ion phase space (left column) at 7.1 MeV/u and (right column) at 10 MeV/u with the nominal beam current of 5 mA within DTL2.

5.1.3 Debunching cavity before injection into carbon synchrotron

To minimize the beam energy spread prior to its injection into the therapy synchrotron, an additional cavity, known as the debunching cavity (DEB), is required.

The optimal position for the DEB is between DTL1 and DTL2. The EM simulations were performed using the Poisson/SUPERFISH codes, and the resulting electric field distribution is presented in Fig. 5.8.

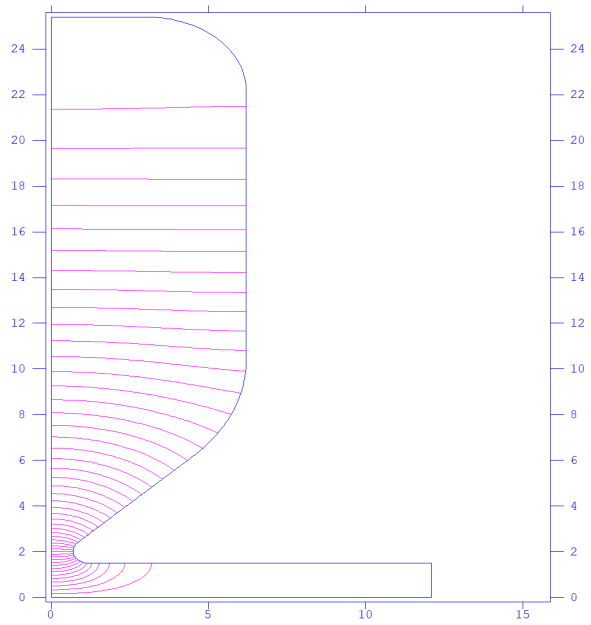


Fig. 5.8. Electric field distribution in DEB used for reducing energy spread of carbon ions before injection into therapy synchrotron, simulated with Poisson/SUPERFISH codes.

The RF and geometry parameters of DEB are summarized in Table 5.5.

Table 5.5. RF and geometry parameters of DEB used for reducing energy spread of carbon ions before injection into therapy synchrotron

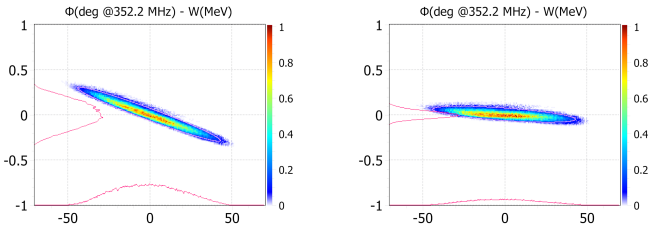
	DEB	**Units**
No. of cells	1	-
Bore radius	15	mm
Length	242	mm
Accelerating field	0.765	MV/m
Nominal tank voltage	130	kV
Power dissipation	17	kW

To assess the impact on beam quality, the energy spread of 95% of the beam and the normalized rms longitudinal emittances at both the entrance and exit of the DEB were computed using TraceWin. These values are provided in Table 5.6.

Table 5.6. Beam parameters of DEB used for reducing energy spread of carbon ions before injection into therapy synchrotron

	DEB	**Units**
Input long. norm. emittance (rms)	1.399	π.deg.MeV
Output long. norm. emittance (rms)	1.403	π.deg.MeV
Input energy spread (for 2σ (95% beam))	$\pm$1.62	%
Output energy spread (for 2σ (95% beam))	$\pm$0.38	%

Given the specific function of the DEB, the longitudinal phase space is the primary area of interest. Therefore, only the longitudinal phase space at both the entrance and exit of the DEB, corresponding to the data in Table 5.6, is shown in Fig. 5.9.



(a) **(b)**

Fig. 5.9. Carbon ion phase space (left column) before and (right column) after DEB.

5.1.4 Comparison and choice of the ideal linac configuration

A detailed study of the IH-DTL operating at 217 MHz has been reported in [43]. Due to the absence of quadrupoles within drift tubes and since it is a π-mode structure, the IH-DTL is 35.1% shorter (corresponding to 1.8 meters) and has almost half the power dissipation (45.7% lower losses) compared to the proposed QA-DTL. However, despite its lower power dissipation and shorter length, the IH-DTL has some disadvantages compared to the QA-DTL. The IH-DTL operates effectively at frequencies below 300 MHz, which excludes the possibility of using klystrons as the RF source, restricting it to the use of SSAs [44]. According to [44], for applications requiring frequencies between 300 MHz and 1 GHz, klystrons are significantly more power efficient than SSAs. As a result, the use of klystrons can significantly reduce the RF

system's cost, making the QA-DTL comparable to the IH-DTL in terms of the overall cost of the RF system. At the exit of the IH-DTL, the longitudinal normalized rms emittance growth of 25.7% has been reported [43], while in the case of the QA-DTL, it is only 2.02%, which demonstrates the strong longitudinal beam control of the QA-DTL over the IH-DTL. On the other hand, the transverse normalized rms emittance growth is comparable for both structures. An overview of parameters concerning the QA-DTL and IH-DTL is shown in Table 5.7.

Table 5.7. Comparison between QA-DTL and IH-DTL for carbon ion acceleration

	Power diss. [kW]	**Power source**	**Length [m]**	**Norm. trans. / long. rms emit. growth [%]**
QA-DTL	626	klystron	5.1	11.2 / 2.02
IH-DTL	340	SSA	3.31	10 / 25.7

Following the first section, the second and third sections accelerate helium ions from 5 MeV/u to 10 MeV/u. In this Thesis, two DTL structures have been chosen for these sections and compared with the IH-DTL structures designed for the same energy range, as presented in [43]. For proper operation, both as a synchrotron injector and for radioisotope production, the IH-DTL requires two debunching cavities with a total power dissipation of 20 kW, and an additional length of 4.6 m [45]. On the other hand, the Alvarez-type linac configuration presented in this Thesis requires only one debunching cavity with a similar power dissipation of 17 kW, which is positioned between DTL cavities, resulting in minimal additional space required. The power dissipation and length of each linac structure, including the estimated length of beam transport lines (BTL) between them, are shown in Table 5.8.

Table 5.8. Comparison between Alvarez-type and H-mode type linac configurations for carbon ion acceleration

	Power diss. [kW]	**Length [m]**
QA-DTL	626	5.1
DTL1 + BTL	181	1.83
DTL2 + BTL	253	2.27
DEB + BTL	17	0.54
Alvarez-type (total)	**1077**	**9.74**
IH-DTL1	340	3.31
IH-DTL2 + BTL	265	1.6
IH-DTL3 + BTL	425	2.04
DEB1 + DEB2 + BTL	20	4.6
H-mode (total)	**1050**	**11.55**

For applications where the ions need to be accelerated beyond 5 MeV/u, as is the case for

the HITRI*plus* linac, the combination of Alvarez-type linac structures is preferable, due to their lower overall length, practically the same total power requirements with a more cost-efficient RF source solution (klystrons over SSAs), and superior longitudinal beam control. The overall layout of the HITRI*plus* linac with DEB, as proposed in this Thesis, is illustrated in Fig. 5.10.

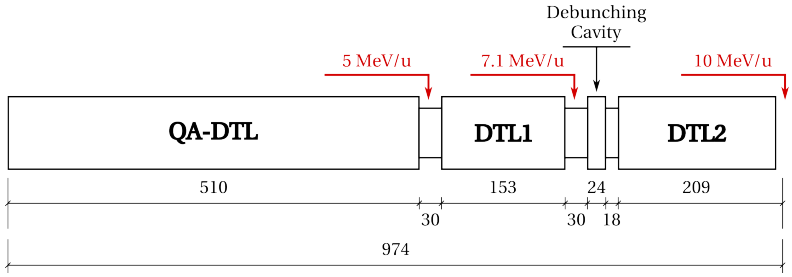


Fig. 5.10. Layout of preferred HITRI*plus* linac configuration. Dimensions are given in cm.

Furthermore, the Alvarez-type linac configuration (QA-DTL for acceleration of low-velocity particles as the first section, and two DTL cavities for further acceleration as the second and third sections) has been chosen by the NIMMS study as its baseline linac, due to its superior longitudinal beam dynamics, and comparable power and length to the H-mode alternative (three IH-DTL cavities for each section).

5.2 NIMMS helium linac designs

The NIMMS helium linac is composed of three distinct linac sections. For the first accelerating stage of the NIMMS linac, the QA-DTL has been chosen, which operates at a frequency of 352.2 MHz. For the second and third sections of the NIMMS linac, two DTL structures were selected to accelerate ions efficiently.

The NIMMS helium linac has to achieve the acceleration of helium ions with a nominal beam current of 5 mA before their injection into a cancer therapy synchrotron. Furthermore, in the case where the NIMMS linac is intended for radioisotope production, it must accommodate a significantly higher beam current of up to 30 mA. The linac has to be capable of accelerating deuterons with a nominal beam current of up to 30 mA, allowing for the production of a wider variety of radioisotopes, as reported in Table 2.1.

In addition to the linac structures, two RF structures for beam manipulation were designed: the Debunching Cavity (DEB) and the Energy Ramping Cavity (ERC). Although the ERC is completely optional, the DEB is a critical component of the system. Both the DEB and ERC were developed and integrated into the NIMMS linac layout.

5.2.1 Quasi-Alvarez Drift Tube Linac for helium injection into synchrotron and radioisotope production

The QA-DTL has been designed to accelerate helium ions with a nominal beam current of 5 mA up to 5 MeV/u, and inject them into the cancer therapy synchrotron. In addition to this, the QA-DTL can also accelerate deuterons or helium ions at higher currents of 30 mA, reaching the same energy of 5 MeV/u, but instead of the synchrotron, the beam is directed to the target for radioisotope production. The RF design of this QA-DTL structure was carried out using the Poisson/SUPERFISH codes, and the electric field distribution within it has been computed (see Fig. 5.11).

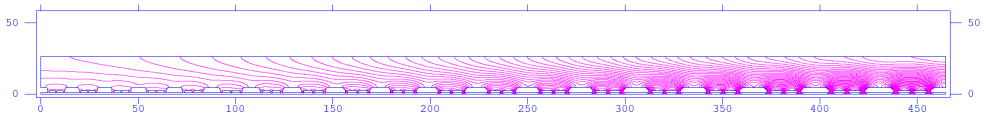


Fig. 5.11. Electric field distribution in QA-DTL for helium ion acceleration from 1 MeV/u to 5 MeV/u, simulated with Poisson/SUPERFISH codes.

The RF and geometry parameters of the QA-DTL are summarized in Table 5.9.

The bore radius of the developed QA-DTL is slightly larger compared to the linac structure designed for the HITRI*plus* project. This increase is necessary to accommodate the acceleration of higher-current beams, resulting in a bore radius of 10 mm and ensuring 100% beam transmission in all examined cases. The beam parameters of the QA-DTL are summarized in Table 5.10.

Table 5.9. RF and geometry parameters of the QA-DTL for acceleration of 5 mA and 30 mA helium ions from 1 MeV/u to 5 MeV/u

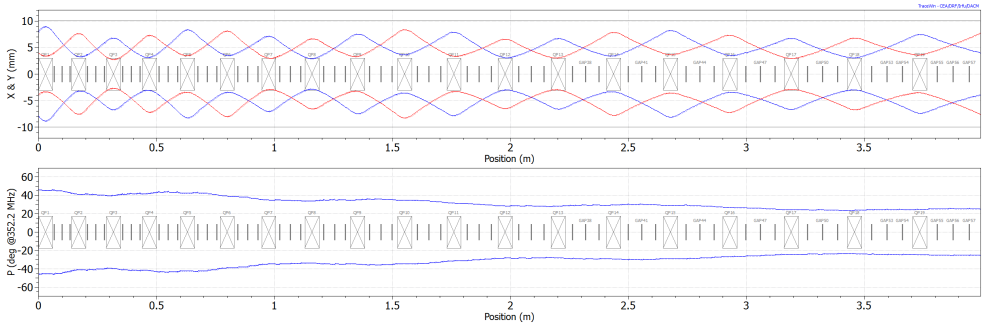
	Synch-rotron	**Radio-isotope**	**Units**
Operating frequency	352.2		MHz
Input energy	4		MeV
Output energy	20		MeV
Peak beam current	5	30	mA
Accelerating field	3.5		MV/m
Synchronous phase	–35 to –24		deg
Length	4.65		m
No. of super-periods	19		-
Effective shunt impedance	60.12		MΩ/m
Power dissipation	570		kW

Table 5.10. Beam parameters of the QA-DTL for helium ion acceleration from 1 MeV/u to 5 MeV/u

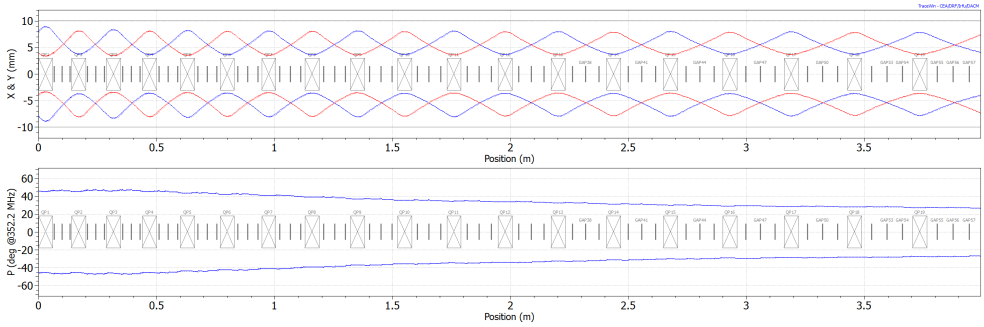
	Synch-rotron	**Radio-isotope**	**Units**
Bore radius	10		mm
Input tran. norm. emittance (rms)(xx')	0.250	0.250	π.mm.mrad
Input tran. norm. emittance (rms)(yy')	0.250	0.250	π.mm.mrad
Output tran. norm. emittance (rms)(xx')	0.257	0.260	π.mm.mrad
Output tran. norm. emittance (rms)(yy')	0.258	0.265	π.mm.mrad
Input long. norm. emittance (rms)	0.394	0.394	π.deg.MeV
Output long. norm. emittance (rms)	0.404	0.419	π.deg.MeV
Energy spread (for 2σ (95% beam))	$\pm$0.97	$\pm$0.94	%
Transmission	100	100	%

The beam envelopes were computed for helium ions used for both synchrotron injection and radioisotope production. These results are illustrated in Fig. 5.12.

The phase space plots in both transverse and longitudinal planes, at the entrance and exit of the QA-DTL, have been computed for 10^5 helium ions. These plots correspond to helium ions used for synchrotron injection at 5 mA (see Fig. 5.13) and for radioisotope production at 30 mA (see Fig. 5.14).

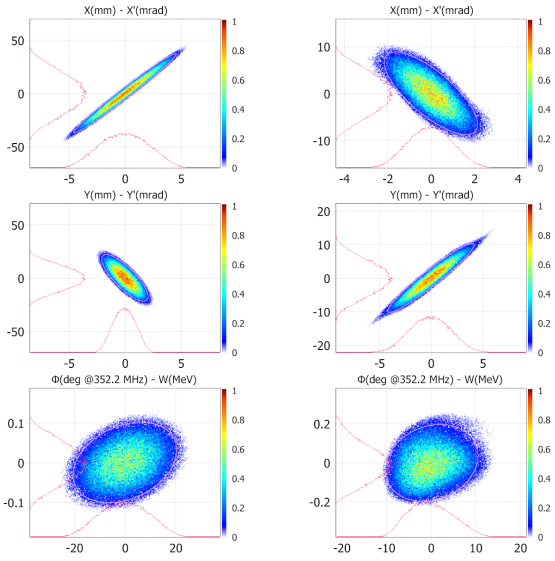


(a)



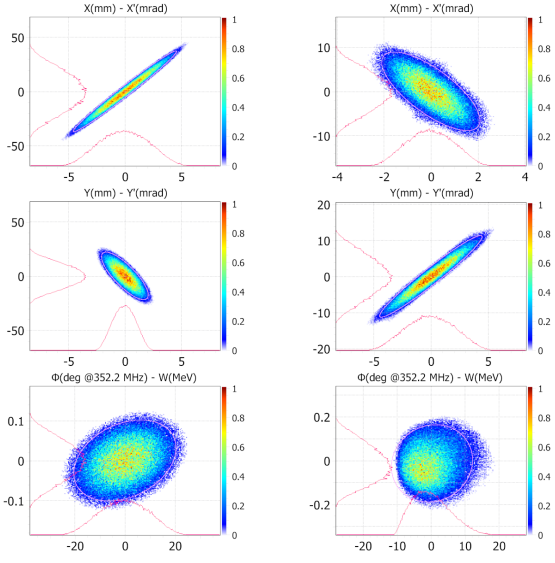
(b)

Fig. 5.12. Beam envelopes along the QA-DTL from 1 MeV/u to 5 MeV/u for helium ions at (a) 5mA (beam for synchrotron) and (b) 30 mA (beam for radioisotope production) of nominal beam current. For each accelerated ion, the top plot represents transverse beam envelopes in the xz and yz planes, while the bottom plot shows the phase envelope.



(a) **(b)**

Fig. 5.13. Helium ion phase space (left column) at 1 MeV/u and (right column) at 5 MeV/u with the nominal beam current of 5 mA within QA-DTL.



(a) **(b)**

Fig. 5.14. Helium ion phase space (left column) at 1 MeV/u and (right column) at 5 MeV/u with the nominal beam current of 30 mA within QA-DTL.

5.2.2 Alvarez Drift Tube Linac for radioisotope production

The QA-DTL is followed by two DTL structures, labeled DTL1 and DTL2, respectively. These structures have been designed with a unique feature: the first cell of each DTL is separated by a copper wall from the following cells.

The electric field distributions inside DTL1 and DTL2, when both of them are excited, have been computed using Poisson/SUPERFISH codes. The first cells of each cavity in this case operate as accelerating cells. The results of the simulation are shown in Fig. 5.15.

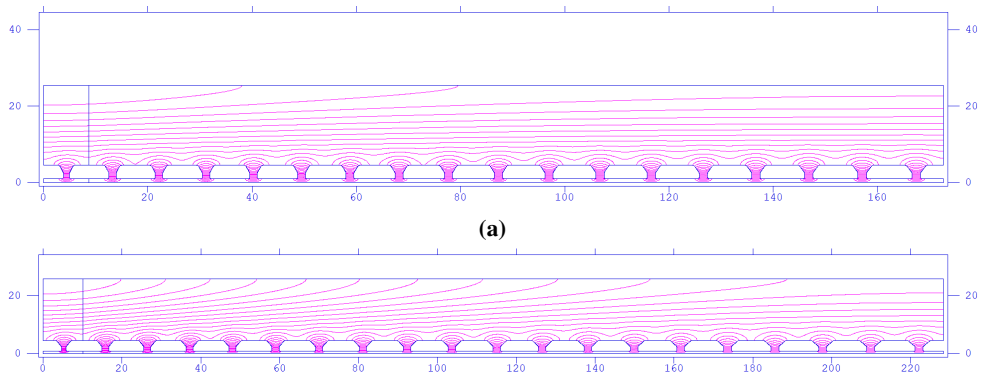


Fig. 5.15. Electric field distribution in (a) DTL1, and (b) DTL2, for acceleration of 30 mA helium ions from (a) 5 MeV/u to 7.1 MeV/u, and (b) 7.1 MeV/u to 10 MeV/u, respectively, simulated with Poisson/SUPERFISH codes.

Table 5.11 summarizes the RF and geometry parameters for the acceleration of 30 mA helium ions within DTL1 and DTL2, from 5 MeV/u to 10 MeV/u. The operating frequency for both structures is 352.2 MHz, with an RF duty cycle of 10%.

Table 5.11. RF and geometry parameters of the DTL1 and DTL2 for acceleration of 30 mA helium ions from 5 MeV/u to 10 MeV/u

	DTL1	DTL2	Units
Operating frequency	352.2		MHz
Input energy	20.0	28.4	MeV
Output energy	28.4	40.0	MeV
Peak beam current	30		mA
Accelerating field	3.1		MV/m
Synchronous phase	–24		deg
Length	1.74	2.28	m
No. of cells	18	20	-
Effective shunt impedance	56.18	59.14	MΩ/m
Power dissipation	235	300	kW

The beam parameters of the DTL1 and DTL2 are presented in Table 5.12.

Table 5.12. Beam parameters of the DTL1 and DTL2 for acceleration of 30 mA helium ions from 5 MeV/u to 10 MeV/u

	DTL1	DTL2	Units
Bore radius	10		mm
Input tran. norm. emittance (rms)(xx')	0.259	0.266	π.mm.mrad
Input tran. norm. emittance (rms)(yy')	0.265	0.272	π.mm.mrad
Output tran. norm. emittance (rms)(xx')	0.267	0.266	π.mm.mrad
Output tran. norm. emittance (rms)(yy')	0.271	0.275	π.mm.mrad
Input long. norm. emittance (rms)	0.421	0.430	π.deg.MeV
Output long. norm. emittance (rms)	0.430	0.516	π.deg.MeV
Energy spread (for 2σ (95% beam))	$\pm$1.09	$\pm$1.01	%
Transmission	100	100	%

The transverse and longitudinal beam envelopes of helium ions, from the entrance of DTL1

(5 MeV/u) to the exit of DTL1 (7.1 MeV/u), at a nominal beam current of 30 mA, are shown in Fig. 5.16.

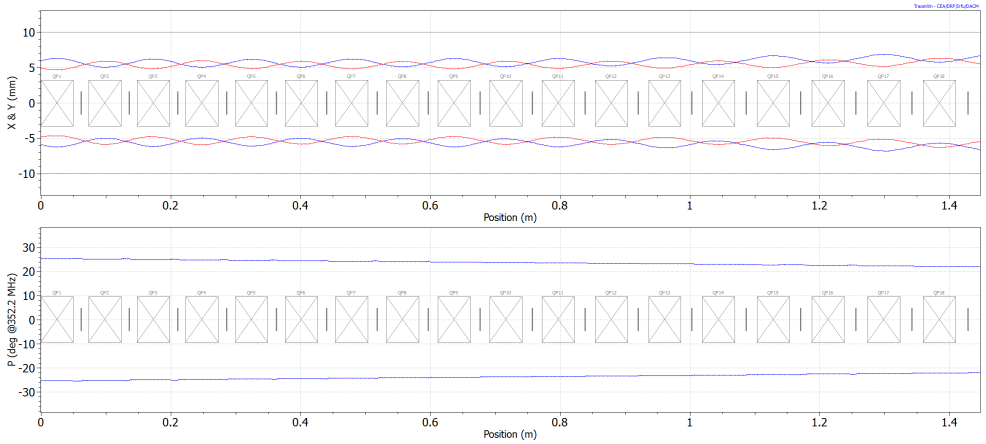


Fig. 5.16. Beam envelopes along the DTL1 from 5 MeV/u to 7.1 MeV/u for helium ions at a beam current of 30 mA. The top plot represents transverse beam envelopes in the xz and yz planes, while the bottom plot shows the phase envelope.

The beam envelopes for helium ions as they are accelerated through DTL2 have been calculated and are illustrated in Fig. 5.17.

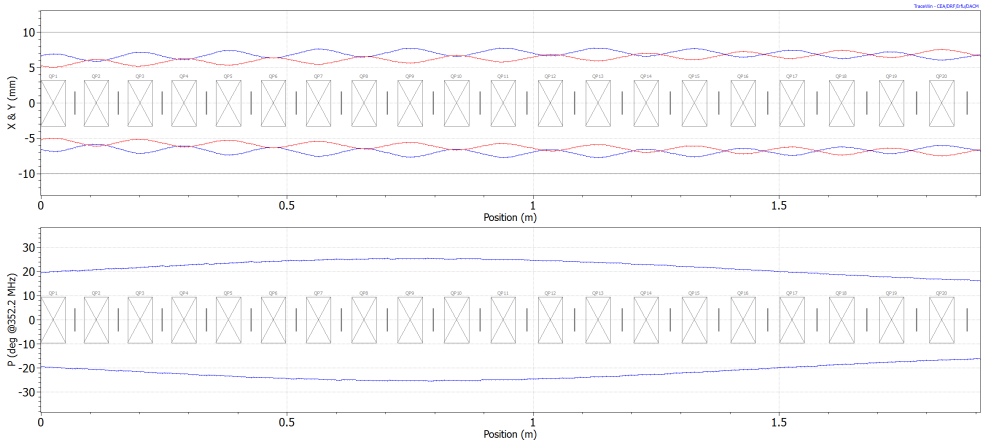
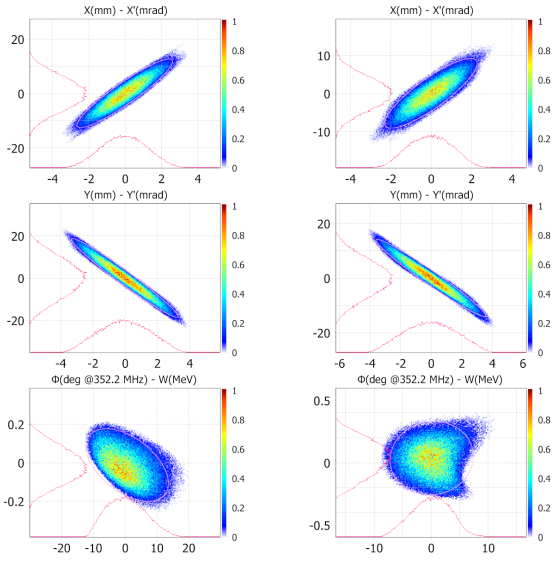


Fig. 5.17. Beam envelopes along the DTL2 from 7.1 MeV/u to 10 MeV/u for helium ions at a beam current of 30 mA. The top plot represents transverse beam envelopes in the xz and yz planes, while the bottom plot shows the phase envelope.

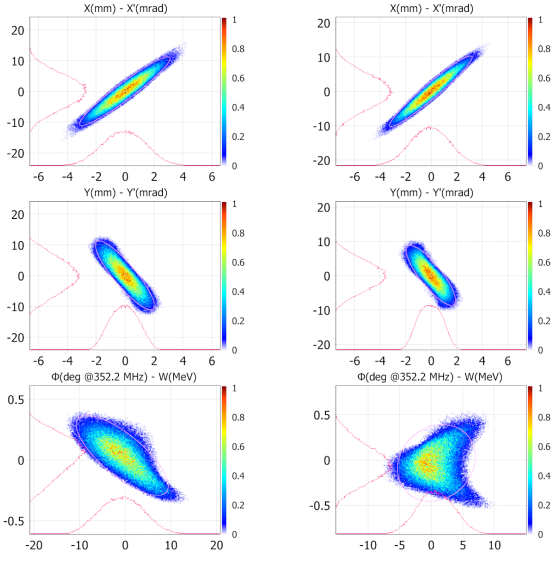
In addition to the beam envelopes, the beam transverse and longitudinal phase space within each structure were also computed. The phase space of the helium ions at a nominal beam current of 30 mA, at both the entrance and exit of DTL1, is presented in Fig. 5.18



(a) **(b)**

Fig. 5.18. Helium ion phase space (left column) at 5 MeV/u and (right column) at 7.1 MeV/u with the nominal beam current of 30 mA within DTL1.

The phase spaces for 30 mA helium ions in both transverse and longitudinal planes at the start and end of DTL2 are shown in Fig. 5.19.



(a) **(b)**

Fig. 5.19. Helium ion phase space (left column) at 7.1 MeV/u and (right column) at 10 MeV/u with the nominal beam current of 30 mA within DTL2.

5.2.3 Debunching cavity and energy ramping cavity before injection into helium synchrotron

For the NIMMS linac, which is designed to inject helium ions into a cancer therapy synchrotron, the inclusion of a debunching cavity (DEB) is essential. Alongside the DEB, an energy ramping cavity (ERC) has been designed as an optional yet valuable addition to the linac configuration. The ERC uses an advanced technique and offers a more efficient beam injection into the synchrotron. However, this comes at the cost of added complexity in the control system. Additionally, to mitigate overall manufacturing costs, both the DEB and ERC have been integrated as part of the DTL1 and DTL2 structures.

In practical terms, the first cell of DTL1 is optimized to serve as an accelerating cell or as the ERC for ramping the energy of particles. This dual-purpose structure significantly complicates the design process but results in a space-saving and cost-effective unit. Similarly, the first cell of the DTL2 can operate either as the DEB or as an accelerating cell. Both the ERC and DEB are isolated from the rest of the accelerating units by copper walls, allowing for independent operation. In other words, when the linac produces radioisotopes, both DEB and ERC function as accelerating cells operating at a synchronous phase along with the rest of the DTL structures, but when the linac injects a beam into the synchrotron, only DEB and ERC are excited at the zero crossing phase while the rest of the DTL structures are off.

The electric field distributions for both cavities are displayed in Fig. 5.20.

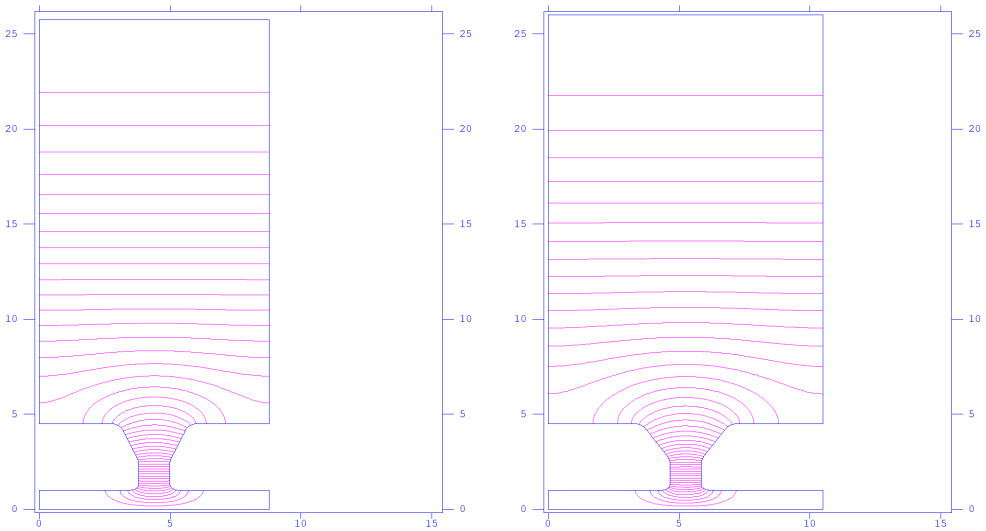


Fig. 5.20. Electric field distribution in (a) ERC used for ramping the energy, and (b) DEB used for reducing energy spread of helium ions before injection into therapy synchrotron, simulated with Poisson/SUPERFISH codes.

In addition to the electric field distributions, the RF and geometry parameters of both

structures are summarized in Table 5.13.

Table 5.13. RF and geometry parameters of ERC used for ramping the energy and DEB used for reducing energy spread of helium ions before injection into therapy synchrotron

	ERC	DEB	Units
No. of cells	1	1	-
Bore radius	10	10	mm
Length	88	105	mm
Accelerating field	3.1	1.4	MV/m
Nominal tank voltage	240	130	kV
Power dissipation	35	8	kW

Following the ERC, the beam undergoes a drift until it reaches the entrance of the DEB, as the DTL1 structure is off during this mode of operation. During the drift through DTL1, the beam becomes elongated but narrower, as shown in Fig. 5.21 (a). As the beam passes through the DEB, the electric field corresponding to the voltage of 130 kV reduces the energy spread by effectively rotating the beam bunch in longitudinal phase space, as illustrated in Fig. 5.21 (b).

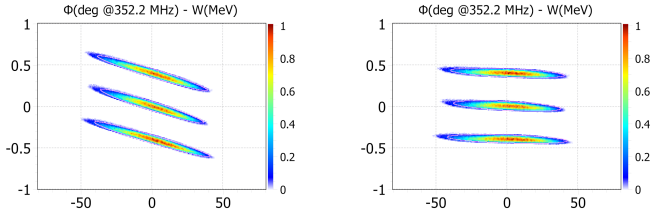


Fig. 5.21. Helium ion phase space (left column) before and (right column) after DEB.

5.2.4 Comparison and choice of the ideal linac configuration

Since the RF costs of QA-DTL are comparable to those of IH-DTL, and the beam dynamics of QA-DTL are superior, the QA-DTL has been chosen as the preferred linac structure for the first section of the NIMMS linac. Despite the beam transmission of 100% in both structures, since the IH-DTL uses KONUS beam dynamics where the majority of the longitudinal period has the synchronous phase of 0 degrees, which is not considered stable motion in the longitudinal phase space [36], the IH-DTL is more prone to beam loss when errors are introduced. Especially at a 10% duty cycle, the beam losses are a concern due to activation and high radioactivity.

For the second and third NIMMS linac sections, two DTL structures have been chosen, as DTL has comparable power requirements to the other linac solutions at energies above 5 MeV/u, with superior beam performance. The power dissipation and length of each linac unit, along with estimated BTL length, are shown in Table 5.14.

Table 5.14. Overview of Alvarez-type linac configuration for helium ion acceleration

	Power diss. [kW]	**Length [m]**
QA-DTL	570	4.65
DTL1 + BTL (with ERC)	235	2.01
DTL2 + BTL (with DEB)	300	2.61
Alvarez-type (total)	**1105**	**9.27**

According to the aforementioned, the final NIMMS linac layout consists of QA-DTL as the first section, DTL1 as the second section, and DTL2 as the third section. The overall layout of the NIMMS linac configuration, consisting of both DEB and ERC cavities, is shown in Fig. 5.22.

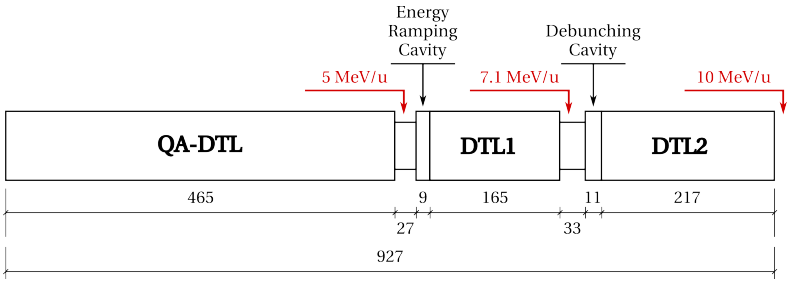


Fig. 5.22. Layout of preferred NIMMS linac configuration. Dimensions are given in cm.

5.3 Isotope production helium linac design

A QA-DTL linac structure specifically devoted to producing one of the most promising alpha-therapy radioisotope, 211-Astatine, has been designed. This QA-DTL is capable of accelerating helium ions with a nominal beam current of 30 mA from 1 MeV/u up to 7.1 MeV/u. Unlike the other linac configurations discussed in this Thesis, this design is not intended to be used as an injector for the cancer therapy synchrotron. The output energy of 7.1 MeV/u (corresponding to a total energy of 28.4 MeV) was chosen to optimize the production of ^{211}At while keeping the energy slightly below the threshold for producing the undesirable ^{210}At, which has a threshold energy of 28.6 MeV [46–48].

The QA-DTL is designed to operate at 352.2 MHz. The EM simulations have been carried out using the Poisson/SUPERFISH codes, computing the electric field distribution within the structure, as shown in Fig. 5.23.

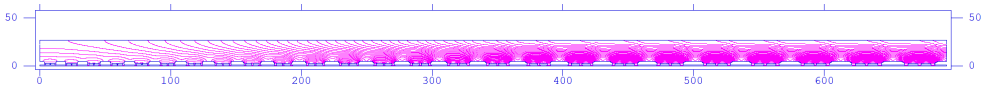


Fig. 5.23. Electric field distribution in QA-DTL for helium ion acceleration from 1 MeV/u to 7.1 MeV/u, simulated with Poisson/SUPERFISH codes.

Table 5.15 presents the RF and geometry parameters of the QA-DTL used for helium ion acceleration from 1 MeV/u to 7.1 MeV/u.

Table 5.15. RF and geometry parameters of the QA-DTL for helium ion acceleration from 1 MeV/u to 7.1 MeV/u

	QA-DTL	**Units**
Operating frequency	352.2	MHz
Input energy	4	MeV
Output energy	28.4	MeV
Peak beam current	30	mA
Accelerating field	3.5	MV/m
Synchronous phase	–35 to –24	deg
Length	6.9	m
No. of super-periods	25	-
Effective shunt impedance	62.18	MΩ/m
Power dissipation	770	kW

Beam dynamics analysis was conducted using the TraceWin code. The simulations ensured 100% helium ion transmission at a nominal beam current of 30 mA. The beam parameters in both

the transverse and longitudinal planes at the entrance and exit of the QA-DTL were successfully computed and are documented in Table 5.16.

Table 5.16. Beam parameters of the QA-DTL for helium ion acceleration from 1 MeV/u to 7.1 MeV/u

	QA-DTL	**Units**
Bore radius	10	mm
Input tran. norm. emittance (rms)(xx')	0.250	π.mm.mrad
Input tran. norm. emittance (rms)(yy')	0.250	π.mm.mrad
Output tran. norm. emittance (rms)(xx')	0.253	π.mm.mrad
Output tran. norm. emittance (rms)(yy')	0.252	π.mm.mrad
Input long. norm. emittance (rms)	0.394	π.deg.MeV
Output long. norm. emittance (rms)	0.406	π.deg.MeV
Energy spread (for 2σ (95% beam))	$\pm$0.69	%
Transmission	100	%

Both the transverse and longitudinal beam envelopes within QA-DTL were computed using TraceWin. The resulting beam envelopes for helium ions at 30 mA are illustrated in Fig. 5.24.

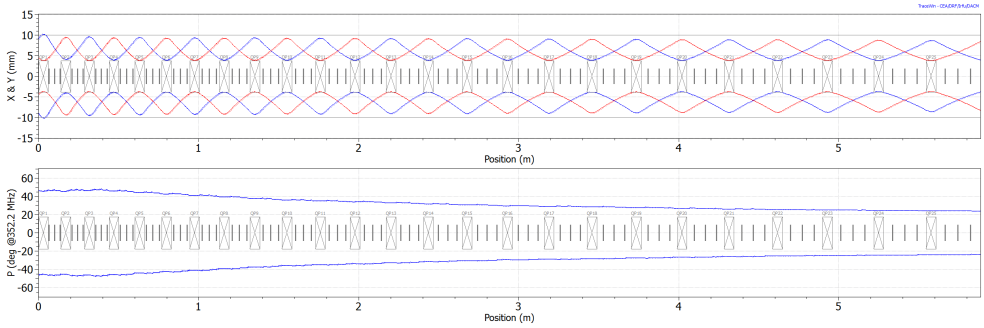


Fig. 5.24. Beam envelopes along the QA-DTL from 1 MeV/u to 7.1 MeV/u with 30 mA of beam current used for radioisotope production. The top plot represents transverse beam envelopes in the xz and yz planes, while the bottom plot shows the phase envelope.

To further describe the beam dynamics, phase space plots for helium ions were created at both the entrance and exit of the QA-DTL, and are presented in Fig. 5.25.

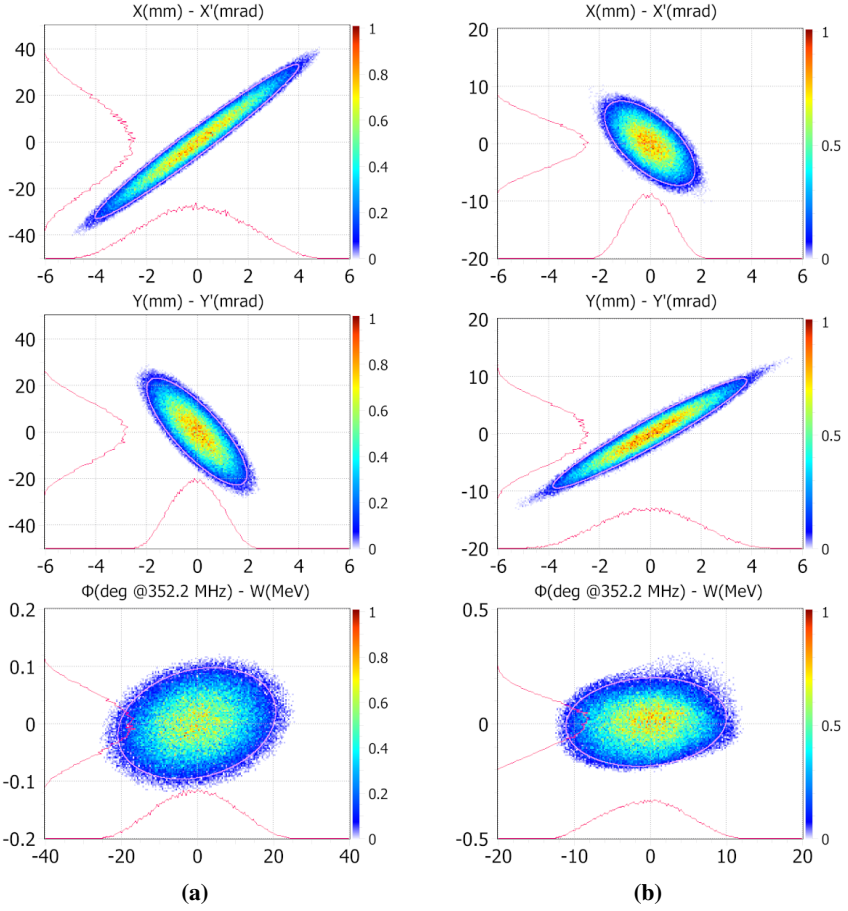


Fig. 5.25. Helium ion phase space (left column) at 1 MeV/u and (right column) at 7.1 MeV/u with the nominal beam current of 30 mA within QA-DTL.

6. Conclusions

The goal of this Thesis was to design linear accelerating structures for the injection of carbon and helium ions at an energy of 5 MeV/u into cancer therapy synchrotrons and the parallel production of radioisotopes with energy up to 10 MeV/u. This goal was successfully achieved by completing the following five tasks:

1. The first task was to **investigate existing ion linac structures** that could be used as a carbon and helium injector for a cancer therapy synchrotron. This was accomplished through an intensive literature analysis, resulting in the identification of twelve distinct linac structures. For low-velocity helium and carbon ion acceleration, two structures were selected for further investigation – namely, Interdigital H-mode Drift Tube Linac (IH-DTL) and Alvarez Drift Tube Linac (DTL). Based on the investigation, it was also proposed that further performance improvements for low-velocity ion injectors of a therapy synchrotron could be achieved by developing a Quasi-Alvarez Drift Tube Linac (QA-DTL), the modification of the DTL, and designing a Separated tanks Interdigital H-mode Drift Tube Linac (S-IH-DTL), the modification of the IH-DTL.

2. The second task was to define an optimization methodology for designing linac accelerating structures, by maximizing power efficiency and ensuring beam transmission without any loss of particles. To achieve this, **optimization algorithms** were developed to maximize the effective shunt impedance per unit length (ZT^2), which is proportional to the power efficiency. Furthermore, the gradient strengths of the permanent magnet quadrupoles, responsible for transverse beam focusing, were optimized to ensure loss-free beam transport within all linac structures.

3. The third task was to **design and optimize different linac structures** with the required input and output parameters, to be used as ion injectors for cancer therapy synchrotrons, or for the production of radioisotopes at different energies. To accomplish this, a new design of QA-DTL was developed. The developed QA-DTL allows ion acceleration at lower energies compared to its predecessor, the DTL. Alongside the QA-DTL, a new S-IH-DTL was designed, while for radioisotope production, a DTL was chosen.

4. The fourth task was to **compare the different linac structures** designed under task three and select the overall best solution for future carbon and helium cancer therapy facilities. The compared linac structures for the acceleration of low-velocity ions were the QA-DTL,

IH-DTL, and S-IH-DTL. Furthermore, for radioisotope production, at energies above 5 MeV/u, the DTL and IH-DTL were compared. All comparisons were based on beam performance, power efficiency, and overall length. Additionally, for low-velocity ion acceleration, a comparison of the total costs between the DTL and QA-DTL was made. A combination of QA-DTL and two DTL cavities was identified as the best linac solution for the future carbon and helium cancer therapy facilities and for the production of a wide range of radioisotopes.

5. Lastly, the fifth task was to **integrate the designed linac structures** into the proposed ion therapy facilities. This was accomplished by integrating the optimized linac solution (the combination of QA-DTL and two DTL cavities) into the general design for both the HITRI*plus* carbon linac and the NIMMS helium linac. Ultimately, due to its demonstrated performance, this configuration was selected as the proposed injector for the future Advanced Particle Therapy Center for the Baltic States [12].

The hypothesis was confirmed by demonstrating a cost-effective and flexible solution for ion acceleration using a linac. Additionally, the results of this Thesis demonstrated that the QA-DTL provides superior beam performance compared to the IH-DTL, thanks to its better focusing lattice (the arrangement of transverse focusing quadrupoles that repeats along the linac structure) and the stable synchronous phase (the phase at which the synchronous particle is aligned with the accelerating field).

6.1 Thesis statements to be defended

1. For the acceleration of low-velocity carbon and helium ions, as an injector for a cancer therapy synchrotron, the developed linac structure (QA-DTL) has 61% lower total costs (cost of the accelerating structure and cost of the RF system) in comparison to the DTL.

2. The developed linac structure is capable of accelerating carbon ions from 0.7 MeV/u, whereas the DTL is capable of accelerating ions from 1 MeV/u at a lower beam current, thus simplifying the preceding accelerating section.

3. The beam within the developed linac structure has more stable longitudinal motion than within the IH-DTL structure currently used in ion therapy, resulting in improved output beam parameters with no beam loss. Specifically, for carbon ion acceleration, comparisons between the QA-DTL and IH-DTL showed significantly lower longitudinal normalized rms emittance growth in favor of the QA-DTL (2.02% vs. 25.7%), while for helium ion acceleration, the QA-DTL also exhibited significantly lower normalized rms emittance growth in the longitudinal plane (2.5% vs. 20.8%).

4. The combination of QA-DTL and two DTL cavities was identified as the best linac solution for integration into future carbon and helium ion therapy facilities and parallel

use in radioisotope production. The combination of the developed QA-DTL and two DTL cavities is shorter (9.74 m vs. 11.55 m), with practically the same power requirements (1077 kW vs. 1050 kW) compared to an IH-DTL based solution.

6.2 Future research challenges

The detailed research presented in this Thesis has provided essential data and laid the groundwork for manufacturing a full-scale short prototype of the QA-DTL, which should be the focus of future research. This prototype should not be intended to accelerate particles, in order to keep costs low, but rather to enable RF measurements and provide an opportunity to explore topics not covered in this thesis, such as investigating post-couplers and field stabilizers, along with developing tuners. Both stabilizers and tuners are crucial for the proper operation of linac structures and must be addressed in future research.

Long DTL and QA-DTL cavities require tight mechanical tolerances to maintain a constant accelerating field along their length. A standard technique to mitigate this sensitivity, and to reduce the machining requirements, involves the use of post-couplers – short metallic posts protruding from the tank toward the drift tubes, alternating from side to side. This stabilization technique improves field flatness by coupling the main accelerating mode with a chain of post-coupler modes, and has to be considered for the QA-DTL.

It is important to mention that the ratio between the cavity radius and the drift tube radius in the developed linac structure is 5.9, which is very close to the value of 5.8 in LINAC4 at CERN [6]. Since the field stabilization of Linac4 was relatively straightforward [49], similar stabilization is expected for the QA-DTL structure. Nevertheless, this must be confirmed through testing on a full-scale prototype of the developed structure. In the event that prototype measurements indicate stabilization issues, the use of a $3/4\lambda$ post-coupler stabilization system, as described in [50], is foreseen.

Additionally, the injector for the linac structure requires further study. More specifically, the ion source and radio frequency quadrupole (RFQ), responsible for pre-acceleration and beam-bunching before the linac structure, should be developed and integrated with the proposed linac configuration. Special attention should be given to the ion source, as a high-current helium beam is required for efficient radioisotope production with the developed QA-DTL linac structure.

BIBLIOGRAPHY

[1] S. Hanna, *RF Linear Accelerators for Medical and Industrial Applications*, 1st. Norwood, MA, USA: Artech House, 2012, p. 210, ISBN: 9781608070909.

[2] U. Amaldi, M. Dosanjh, J. Balosso, J. Overgaard, and B. Sørensen, "A facility for tumour therapy and biomedical research in south-eastern Europe," *CERN Yellow Reports: Monographs*, no. CERN-2019-002, 2019. DOI: 10.23731/CYRM-2019-002.

[3] M. Benedikt, J. Gutleber, U. Dorda, A. Fabich, M. Palm, and W. Pirkl, "Overview of the MedAustron design and technology choices," CERN, Geneva, Switzerland, Tech. Rep. CERN-ATS-2010-116, 2010.

[4] U. Scheeler *et al.*, "Recommissioning of the Marburg ion-beam therapy centre (MIT) accelerator facility," in *Proc. 7th International Particle Accelerator Conference (IPAC'16)*, JACoW Publishing, 2016, pp. 1908–1910. DOI: 10.18429/JACoW-IPAC2016-TUPOY004.

[5] B. Schlitt *et al.*, "Commissioning and operation of the injector Linacs for HIT and CNAO," in *Proc. 24th International Linear Accelerator Conference (LINAC'08)*, JACoW Publishing, 2008, pp. 720–724.

[6] M. Vretenar *et al.*, *Linac4 Design Report* (CERN Yellow Reports: Monographs). Geneva: CERN, Sep. 2020, vol. 6/2020. DOI: 10.23731/CYRM-2020-006.

[7] M. Okamura *et al.*, "A new medium energy beam transport line for the proton injector of AGS-RHIC," in *Proc. 25th International Linear Accelerator Conference (LINAC'10)*, Tsukuba, Japan: JACoW Publishing, 2010, pp. 458–460.

[8] R. Garoby *et al.*, "The European spallation source design," *Physica Scripta*, vol. 93, no. 1, p. 014 001, 2017. DOI: 10.1088/1402-4896/aa9bff.

[9] HITRIplus Consortium, *Heavy ion therapy research integration plus (HITRIplus), grant agreement ID 101008548*, European Commission, CORDIS project page, 2023. [Online]. Available: https://cordis.europa.eu/project/id/101008548.

[10] M. Rabiei, M. Asadi, and H. Yousefnia, "Astatine-211 radiopharmaceuticals: Status, trends, and the future," *Current Radiopharmaceuticals*, vol. 17, no. 1, pp. 7–13, 2024. DOI: 10.2174/0118744710262325231025075638.

[11] CERN – Conseil Européen pour la Recherche Nucléaire, *Next ion medical machine study (NIMMS)*, Project website, CERN, 2025. [Online]. Available: https://nimms.web.cern.ch.

[12] K. Paļskis *et al.*, "Particle therapy – future for the Baltic states? synthesis of the expert workshop report," *Health and Technology*, vol. 14, no. 5, pp. 965–972, 2024. DOI: 10.1007/s12553-024-00875-2.

[13] International Atomic Energy Agency, *Cyclotron Produced Radionuclides: Physical Characteristics and Production Methods* (Technical Reports Series 468). Vienna, Austria: International Atomic Energy Agency, 2009, ISBN: 978-92-0-106908-5.

[14] J. C. Clark and D. J. Silvester, "A cyclotron method for the production of fluorine-18," *The International Journal of Applied Radiation and Isotopes*, vol. 17, no. 3, pp. 151–154, 1966. DOI: 10.1016/0020-708X(66)90034-4.

[15] V. Casella, T. Ido, A. P. Wolf, J. S. Fowler, R. R. MacGregor, and T. J. Ruth, "Anhydrous F-18 labeled elemental fluorine for radiopharmaceutical preparation," *Journal of Nuclear Medicine*, vol. 21, no. 8, pp. 750–757, 1980.

[16] A. Hermanne, F. Tárkányi, S. Takács, S. F. Kovalev, and A. Ignatyuk, "Activation cross sections of the ^{64}Ni(d,2n) reaction for the production of the medical radionuclide ^{64}Cu," *Nuclear Instruments and Methods in Physics Research Section B: Beam Interactions with Materials and Atoms*, vol. 258, no. 2, pp. 308–312, 2007. DOI: 10.1016/j.nimb.2007.02.071.

[17] Y. Skakun and S. M. Qaim, "Excitation function of the ^{64}Ni(α,p)^{67}Cu reaction for production of ^{67}Cu," *Applied Radiation and Isotopes*, vol. 60, no. 1, pp. 33–39, 2004. DOI: 10.1016/j.apradiso.2003.09.003.

[18] I. Kambali and F. A. Wibowo, "Comparison of Gallium-68 production yields from (p,2n), (α,2n) and (p,n) nuclear reactions applicable for cancer diagnosis," in *Journal of Physics: Conference Series*, vol. 1198, IOP Publishing, 2019, pp. 1–10. DOI: 10.1088/1742-6596/1198/2/022003.

[19] A. M. La Gamma and S. J. Nassiff, "Excitation functions for deuteron-induced reactions on ^{89}Y," *Radiochimica Acta*, vol. 19, no. 4, pp. 161–162, 1973. DOI: 10.1524/ract.1973.19.4.161.

[20] S. Manenti *et al.*, "Excitation function and yield for the ^{103}Rh(d,2n)^{103}Pd nuclear reaction: Optimization of the production of Palladium-103," *Nuclear Medicine and Biology*, vol. 49, pp. 30–37, 2017. DOI: 10.1016/j.nucmedbio.2017.02.005.

[21] A. Nikjou and M. Sadeghi, "Overview and evaluation of different nuclear level density models for the ^{123}I radionuclide production," *Applied Radiation and Isotopes*, vol. 136, pp. 45–58, 2018. DOI: 10.1016/j.apradiso.2018.02.003.

[22] S. Takács *et al.*, "Excitation function of ^{122}Te(d,n)^{123}I nuclear reaction: Production of ^{123}I at a low energy cyclotron," *Applied Radiation and Isotopes*, vol. 50, no. 3, pp. 535–540, 1999. DOI: 10.1016/S0969-8043(98)00059-1.

[23] I. Kambali, "Production of Lu-177 radionuclide using deuteron beams: Comparison between (d,n) and (d,p) nuclear reactions," in *Journal of Physics: Conference Series*, vol. 1120, IOP Publishing, 2018, pp. 1–7. DOI: 10.1088/1742-6596/1120/1/012011.

[24] S. Lahiri and M. Maiti, "Recent developments in nuclear data measurements and chemical separation methods in accelerator production of astatine and technetium radionuclides," *Radiochimica Acta*, vol. 100, no. 8–9, pp. 535–541, 2012. DOI: 10.1524/ract.2011.1888.

[25] M. R. Zalutsky and M. Pruszynski, "Astatine-211: Production and availability," *Current Radiopharmaceuticals*, vol. 4, no. 3, pp. 177–185, 2011. DOI: 10.2174/1874471011104030177.

[26] G. Moffitt, *Medical radioisotope production platform*, Presentation, Nusano, 2023. [Online]. Available: https://nusano.com/wp-content/uploads/2023/05/Nusano_At211_COSTMeeting_webpub.pdf.

[27] N. B. Smith and A. Webb, *Introduction to Medical Imaging: Physics, Engineering and Clinical Applications*. Cambridge, UK: Cambridge University Press, 2010, ISBN: 978-0-521-19065-7.

[28] M. A. Flower, *Webb's Physics of Medical Imaging*, 2nd. Boca Raton, FL, USA: CRC Press, 2012, ISBN: 978-0-7503-0573-0.

[29] F. F. Knapp and A. Dash, *Radiopharmaceuticals for Therapy*. New Delhi, India: Springer, 2016, ISBN: 978-81-322-2606-2. DOI: 10.1007/978-81-322-2607-9.

[30] D. M. Pozar, *Microwave Engineering*, 4th. Hoboken, NJ, USA: Wiley, 2012, ISBN: 978-0-470-63155-3.

[31] C. A. Balanis, *Balanis' Advanced Engineering Electromagnetics*, 3rd. Hoboken, NJ, USA: John Wiley & Sons, 2024, ISBN: 978-1-394-18095-2.

[32] T. P. Wangler, *RF Linear Accelerators*, 2nd. Weinheim, Germany: Wiley-VCH, 2008, ISBN: 978-3-527-40680-7. DOI: 10.1002/9783527623426.

[33] M. Vretenar, "Low-beta structures," in *CAS — CERN Accelerator School: RF for Accelerators*, Geneva, Switzerland: CERN, 2011, pp. 319–340. DOI: 10.5170/CERN-2011-007.319.

[34] M. R. Khalvati, V. Bencini, and S. Ramberger, "Quasi-Alvarez drift-tube Linac structures for heavy ion therapy accelerator facilities," *Physical Review Accelerators and Beams*, vol. 26, no. 2, p. 022 001, 2023. DOI: 10.1103/PhysRevAccelBeams.26.022001.

[35] J. M. Garland, J.-B. Lallement, and A. Lombardi, "LINAC5 – a Quasi-Alvarez Linac for BioLEIR," in *Journal of Physics: Conference Series*, vol. 874, IOP Publishing, 2017, p. 012 057. DOI: 10.1088/1742-6596/874/1/012057.

[36] R. Tiede, U. Ratzinger, H. Podlech, C. Zhang, and G. Clemente, "KONUS beam dynamics designs using H-mode cavities," in *Proc. 42nd ICFA Advanced Beam Dynamics Workshop on High-Intensity, High-Brightness Hadron Beams (HB'08)*, JACoW Publishing, 2008, pp. 223–230.

[37] Los Alamos National Laboratory, *Los alamos national laboratory (LANL)*, Laboratory website, 2025. [Online]. Available: https://www.lanl.gov.

[38] M. T. Menzel and H. K. Stokes, *User's guide for the POISSON/SUPERFISH group of codes*, English, Report LA-UR-87-115, Los Alamos National Laboratory (LANL), Los Alamos, NM, USA, Jan. 1987, 207 pp.

[39] Dassault Systèmes Simulia Corp., *CST Studio Suite: 3d EM simulation and analysis software*, Computer software, Dassault Systèmes, Vélizy-Villacoublay, France, 2025.

[40] D. Uriot and N. Pichoff, *TraceWin: Beam dynamics simulation code for linear accelerators*, Computer software, Commissariat à l'énergie atomique et aux énergies alternatives (CEA), Saclay, France, 2025.

[41] J. H. Billen, *SFCODES2: Auxiliary codes for the POISSON/SUPERFISH group of programs*, English, Version 7.17, Los Alamos National Laboratory (LANL), Los Alamos, NM, USA, Jan. 2006, 64 pp.

[42] M. M. Alauddin, "Positron emission tomography (PET) imaging with ^{18}F-based radiotracers," *American Journal of Nuclear Medicine and Molecular Imaging*, vol. 2, no. 1, pp. 55–76, 2011.

[43] U. Ratzinger, B. Koubek, H. Höltermann, H. Podlech, and M. Vretenar, "Linac design within HITRIplus for particle therapy," *JACoW LINAC*, vol. 2022, pp. 134–137, 2022. DOI: 10.18429/JACoW-LINAC2022-MOPOGE01.

[44] J. C. Whitaker, *The RF Transmission Systems Handbook*. Boca Raton, FL, USA: CRC Press, 2002, ISBN: 978-0-8493-0973-1.

[45] U. Ratzinger, "H-type Linac structures," in *CAS — CERN Accelerator School: Radio Frequency Engineering*, Geneva, Switzerland: CERN, 2005, pp. 351–378. DOI: 10.5170/CERN-2005-003.351.

[46] T. Bigourdan, A. Cadiou, A. Guertin, and F. Haddad, "Discussions on liquid bismuth target use as an alternative for astatine-211 production," in *EPJ Web of Conferences*, vol. 285, EDP Sciences, 2023, p. 09 002. DOI: 10.1051/epjconf/202328509002.

[47] A. Hermanne, F. Tárkányi, S. Takács, Z. Szücs, Y. N. Shubin, and A. I. Dityuk, "Experimental study of the cross-sections of α-particle induced reactions on ^{209}Bi," *Applied Radiation and Isotopes*, vol. 63, no. 1, pp. 1–9, 2005. DOI: 10.1016/j.apradiso.2005.01.015.

[48] M. Maiti, S. Lahiri, D. Kumar, and D. Choudhury, "Separation of no-carrier-added astatine radionuclides from α-particle irradiated lead bismuth eutectic target: A classical method," *Applied Radiation and Isotopes*, vol. 127, pp. 227–230, 2017. DOI: 10.1016/j.apradiso.2017.06.020.

[49] M. R. Khalvati and S. Ramberger, "Tuning and field stabilization of the CERN Linac4 drift tube Linac," CERN, Geneva, Switzerland, Tech. Rep. CERN-ACC-2014-0167, 2014.

[50] M. Vretenar and D. J. Warner, "Field stabilization in the Quasi-Alvarez structure," in *Proc. 15th Linear Accelerator Conference (LINAC'90)*, Albuquerque, NM, USA: JACoW Publishing, 1990, pp. 96–98.



Lazar Nikitović was born in 1994 in Cetinje, Montenegro. He obtained his Bachelor's degree (2016), Specialist degree (2017), and Master's degree (2020) in Electrical Engineering from the University of Montenegro. From the beginning of 2022 until the end of 2024, he was enrolled in the Doctoral Student Programme at CERN, where he worked on the development of linear accelerators for medical applications. From 2025 to 2026, he was a researcher at the Institute of Particle Physics and Accelerator Technologies, Faculty of Natural Sciences and Technology, Riga Technical University (RTU). His research interests are radio frequency (RF) engineering and accelerator technologies.